AGU PUBLICATIONS

JGR

Journal of Geophysical Research: Oceans

RESEARCH ARTICLE

10.1002/2013JC008908

**Key Points:**

- Local atmospheric variability modulates the structure of the ACC south of Africa
- Positive SAM is linked with a warmer ACC and lower (higher) SAF (APF) transport
- The SAF (APF) location south of Africa is not linked to the local wind forcing

**Correspondence to:**
R. Domingues,
Ricardo.Domingues@noaa.gov

**Citation:**
Domingues, R., G. Goni, S. Swart, and S. Dong (2014), Wind forced variability of the Antarctic Circumpolar Current south of Africa between 1993 and 2010, *J. Geophys. Res. Oceans*, *119*, 1123–1145, doi:10.1002/2013JC008908.

Received 5 MAR 2013
Accepted 12 JAN 2014
Accepted article online 16 JAN 2014
Published online 18 FEB 2014

# Wind forced variability of the Antarctic Circumpolar Current south of Africa between 1993 and 2010

**Ricardo Domingues[1,2], Gustavo Goni[2], Sebastiaan Swart[3,4], and Shenfu Dong[1,2]**

[1]Cooperative Institute for Marine and Atmospheric Studies, University of Miami, Miami, Florida, USA, [2]Atlantic Oceanographic and Meteorological Laboratory, NOAA, Miami, Florida, USA, [3]Southern Ocean Carbon and Climate Observatory, CSIR – NRE, Stellenbosch, South Africa, [4]Department of Oceanography, Marine Research Institute, University of Cape Town, Cape Town, South Africa

**Abstract** The variability of the Antarctic Circumpolar Current (ACC) system is largely linked to the atmospheric forcing. The objective of this work is to assess the link between local wind forcing mechanisms and the variability of the upper-ocean temperature and the dynamics of the different fronts in the ACC region south of South Africa. To accomplish this, in situ and satellite-derived observations are used between 1993 and 2010. The main finding of this work is that meridional changes in the westerlies linked with the Southern Annular Mode (SAM) drive temperature anomalies in the Ekman layer and changes in the Subantarctic Front (SAF) and Antarctic Polar Front (APF) transports through Ekman dynamics. The development of easterly anomalies between 35°S and 45°S during positive SAM is linked to reduced (increased) SAF (APF) transports and a warmer mixed layer in the ACC. The link between the changes in the wind stress and the SAF and APF transport variations occurs through the development of Ekman pumping anomalies near the frontal boundaries, driving an opposite response on the SAF and APF transports. The observed wind-driven changes in the frontal transports suggest small changes to the net ACC transport. In addition, observations indicate that the SAF and APF locations in this region are not linked to the local wind forcing, emphasizing the importance of other factors (e.g., baroclinic instabilities generated by bottom topography) to changes in the frontal location. Results obtained here highlight the importance of repeat XBT temperature sections and their combined analysis with other in situ and remote sensing observations.

## 1. Introduction

The Antarctic Circumpolar Current (ACC) is a major conduit for interoceanic exchange of heat and salt that is largely driven by the midlatitude westerly winds. Because climate change in the Southern Hemisphere has been marked by the strengthening and the southward displacement of the circumpolar westerlies [*Thompson and Solomon*, 2002], there is an active debate on the response of the ACC to these changes. While some climate model studies show that the intensification of the westerlies may drive an increase of the ACC transport [*Bi et al*., 2002; *Saenko et al*., 2005; *Fyfe and Saenko*, 2006], other model studies show no change [*Hallberg and Gnanadesikan*, 2006; *Meredith and Hogg*, 2006; *Hogg et al*., 2008; *Screen et al*., 2009] or even a reduction [*Yang et al*., 2008; *Wang et al*., 2011] in the transport of this current. On interannual time scales, the high-resolution simulations exhibit an "eddy saturated" ocean state in response to the increase in the wind stress, which does not affect the total circumpolar transport, but enhances the eddy field, driving an increase in the poleward heat flux [*Meredith and Hogg*, 2006; *Hogg et al*., 2008]. In addition, recent observations show that there has been no increase in the tilt of density surfaces in the ACC [*Boning et al*., 2008], which indicates that the ACC transport is insensitive to changes in the wind stress on decadal time scales. These studies, however, analyzed an averaged response of the ACC to changes in the westerlies, while a large portion of the ACC variability is determined by the individual behavior of the ACC fronts [*Swart and Speich*, 2010]. Because changes in the dynamics of the ACC are attributed to the warming of the Southern Ocean [*Gille*, 2002, 2008], the evaluation of the specific response of the ACC fronts to the changes in the atmospheric forcing is crucial.

The main fronts associated with the ACC are termed as follows: the Subtropical Front (STF), the Subantarctic Front (SAF), the Antarctic Polar Front (APF), the Southern ACC Front (sACCf), and the Southern Boundary of the ACC (SBdy). It is recognized that the SAF and the APF are the more dominant of these fronts [*Legeais*

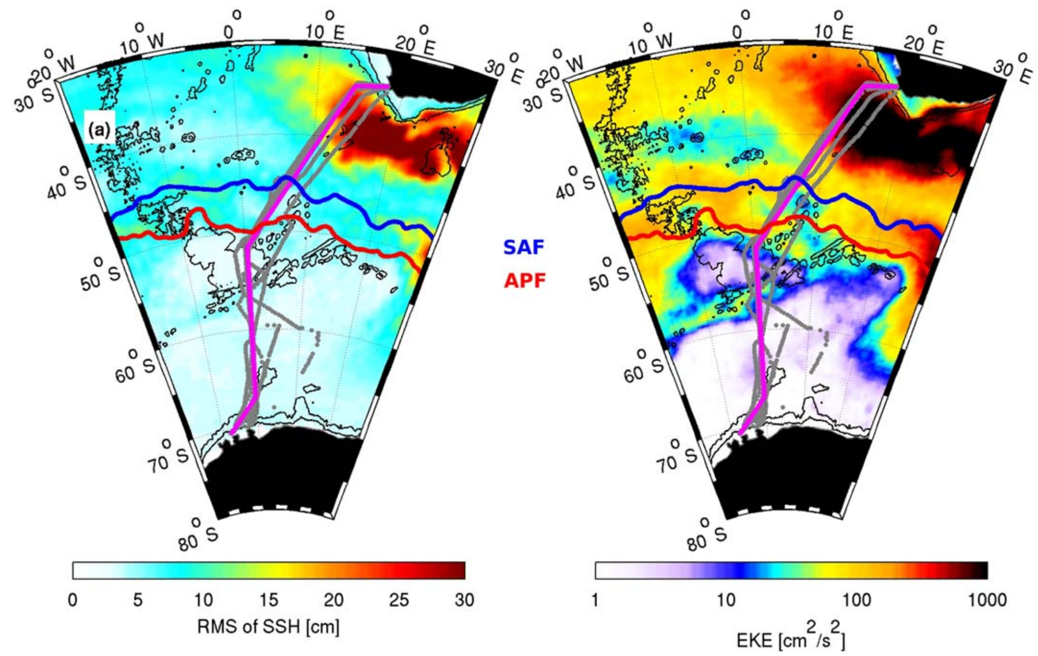


**Figure 1.** Altimetry-derived (a) RMS of Sea Surface Height (SSH) and (b) the Eddy Kinetic Energy (EKE) between 1993 and 2010. Overlaid on the fields are the locations of the 16 AX25 XBT realizations (gray lines), the position of the reference transect used in this work (thick magenta line), the 1000 m and 3000 m isobaths (thin black lines), and the average SAF (blue line) and APF (red line) location during 1993–2010 based on geostrophic velocity from altimetry.

*et al*., 2005; *Dong et al*., 2006; *Sallee et al*., 2008], since they represent up to 75% of the total mass transport of the ACC [*Rintoul and Sokolov*, 2001; *Swart et al*., 2008]. Because of the different latitudinal ranges, the SAF and APF are exposed to different Ekman regimes [*Sallee et al*., 2008], suggesting that these two fronts may respond differently to changes in the wind stress.

Although observations suggest that the ACC transport is insensitive to the trends in the winds, the wind stress variability causes adjustments in the ACC structure through changes in the frontal transports [*Wearn and Baker*, 1980; *Gille* et al., 2001] and locations [*Sallee et al*., 2008]. While the link between changes in the local wind stress and in the ACC frontal transports is still to be assessed, previous studies demonstrated that frontal motions are largely driven by the wind forcing in the absence of topographic steering [*Sallee et al*., 2008; *Billany et al*., 2010]. Wind stress anomalies associated with the Southern Annular Mode (SAM), which is the dominant mode of atmospheric variability in the Southern Hemisphere [*Thompson and Wallace*, 2000], drive frontal motions in most of the Southern Ocean [*Sallee et al*., 2008]. For example, poleward movement of the ACC fronts is observed in the Indian Basin during a positive phase of the SAM, while equatorward displacement is observed in the Pacific [*Sallee et al*., 2008]. Positive SAM phases drive changes in the wind pattern in the Southern Ocean by shifts in the atmospheric mass, which lead to westerly (easterly) zonal geostrophic wind anomaly south (north) of 45°S, causing an immediate dynamic response of the ocean through meridional Ekman transport [*Gupta and England*, 2006]. These Ekman transport anomalies lead to convergent/divergent regions in the Southern Ocean [*Hall and Visbeck*, 2002] that may also potentially affect the frontal transports.

The region of the Southern Ocean between Africa and Antarctica provides a suitable scenario for evaluating the link between local wind stress variability and frontal transports of the SAF and APF. This is due to the significant observational effort that has been conducted in the region to investigate the Atlantic-Indian water mass and heat exchanges [*Ansorge et al*., 2005; *Gladyshev et al*., 2008]. Within this context, a high-density transect between South Africa and Antarctica (AX25, Figure 1) was implemented as part of the Expendable Bathythermograph (XBT) Program at the Atlantic Oceanographic and Meteorological Laboratory of the National Oceanic and Atmospheric Administration (AOML/NOAA) in cooperation with scientists at the University of Cape Town, South Africa. The AX25 line provides high-quality subsurface temperature observations that can be used along with altimetry observations (the transect primarily follows a Jason-1 altimeter track until the Greenwich Meridian) to provide an integrated analysis between the variability of the SAF and APF transports [*Swart et al*., 2008] and the thermal structure in the ACC [*Swart et al*., 2010; *Swart and Speich*, 2010]. Therefore, the goals of this study are to (i) assess the upper-ocean temperature variability between South Africa and Antarctica, (ii) assess the variability of the SAF and APF transports and locations, and (iii) understand whether the local atmospheric forcing drives changes in the ACC region south of Africa. Focus is given to the ocean variability forced by meridional changes in the structure of the westerlies. To accomplish this, the following data sets are analyzed for the period between 1993 and 2010: (a) 16 XBT temperature sections, (b) Argo float and CTD temperature-salinity (T-S) profiles, (c) satellite sea surface temperature (SST), (d) satellite sea surface height (SSH), (e) satellite ocean wind, and (f) atmospheric SAM index. This manuscript is organized as follows: section 2 describes the data sets employed; in section 3, the methods employed are shown; in section 4, the results from the observations are explained, while in section 5 the possible links between the atmospheric and frontal variability are addressed, and finally, in section 6, conclusions are drawn.

## 2. Data

### 2.1. Temperature Sections

High-density XBT transects provide a snapshot of the synoptic upper-ocean thermal structure, and are used in this study to: (1) evaluate the variability of the subsurface temperature structure of the upper-ocean between South Africa and Antarctica; (2) define the location of the SAF and APF; and (3) investigate the baroclinic transport variability of these two fronts.

The AX25 XBT repeat transect (also known as the GoodHope line) was implemented in February 2004 and 16 sections were collected until February 2011 (Figure 1). Two realizations are generally carried out per year during austral summer: one at the very beginning of the season (November/December), and the second one at the end of the season (January/February). One additional transect was performed during the spring (October) of 2005. South of Africa, XBTs are deployed every 20 to 30 km along AX25 between 35°S and 70°S, and on average, approximately 180 probes are used on each occupation. From the 16 transects, 5 (November 2004, January 2005, October 2005, December 2007, and March 2008) did not cover the entire AX25 due to harsh weather or due to the presence of sea-ice. The XBTs provide temperature measurements from the surface to approximately 800 m, with an accuracy of about 0.15°C. Quality control is applied to raw temperature data, and questionable profiles are discarded [*Bailey et al*., 1994; *Daneshzadeh et al*., 1994]. Further details on each AX25 occupation can be found at: www.aoml.noaa.gov/phod/hdenxbt.

Individual temperature sections are interpolated onto a reference section, with standard depths every 0.5 m, and a fixed 10 km spacing along the track. Most of the XBT transects occurred at or in close proximity to the "reference transect" (Figure 1). However, during the February 2006 and December 2009 realizations, the vessel took alternate routes south of 55°S that separated from the reference transect by approximately 200 km zonally. The sections produced by the alternate routes are also considered in this work, since these zonal displacements south of 55°S are not expected to introduce significant error because the SAF and APF are located to the north of this latitude.

### 2.2. Argo and CTD-Derived Temperature and Salinity Profiles

In addition to the XBT data, Argo and CTD-derived T-S profiles are used here to (1) analyze the variability of temperature in the upper-ocean, in particular during winter months when XBT data are not available, and to (2) derive empirical relationships to estimate the SAF and APF transports [*Swart et al*., 2008]. A total of 1936 profiles from the period of 2002–2010 were retrieved within an area 2° east and west of the AX25 reference transect (Figure 1). These profiles correspond to the Delayed Time mode (DT) data from the Global Temperature-Salinity Profile Program (GTSPP; http://www.nodc.noaa.-gov/GTSPP). A few real time profiles, which were not included in the DT data, were added following the standard quality control procedures approved by the international Argo data management [*Schmid*, 2005]. From the 1936 profiles used in this work, 1398 were sampled during nonsummer months.

In this study, the bottom depth is used as the reference level in computing transports. Therefore, to obtain absolute dynamic heights from the Argo and CTD profiles, the T-S-derived dynamic height referenced to 1800 m is added to the absolute dynamic height at 1800 m from the International Pacific Research Center

(IPRC) climatology (available at http://iprc.soest.hawaii.edu). This climatology is based on in situ T-S profiles and satellite altimetry and is available at 27 standard vertical levels with a 1° spatial resolution.

### 2.3. Sea Surface Temperature

The XBT temperature sections provide measurements of the subsurface structure of the upper-ocean between South Africa and Antarctica, while the satellite SST data are also used in this study to assess the temporal variability of the temperature at the surface. Daily Optimally Interpolated Sea Surface Temperature, Version 2 (OISST.v2) from NOAA/OAR/ESRL/PSD (available at http://www.esrl.noaa.gov/psd/) data for the period 1993–2010 are used in this study. This product combines in situ and satellite temperature observations through an objective analysis scheme [*Reynolds et al*., 2007] and has a 0.25° spatial resolution.

### 2.4. Wind Fields

Wind stress data are used in this work to: (1) assess the local atmospheric variability south of Africa and (2) investigate the link between the atmospheric forcing and the SAF and APF variability. The cross-calibrated multiplatform ocean surface wind velocity product (CCMP) available at NASA's Physical Oceanography Distributed Active Archive Center (PODAAC, available at http://podaac.jpl.nasa.gov/) is used here. This product combines all available ocean surface wind observations from SSM/I, AMSR-E, TMI, QuikSCAT and Sea-Winds, and spans back to 1987 with a 6 h and 25 km resolution [*Atlas et al*., 2011]. Five day composites are obtained for the area between 70°S–35°S and 10°W–20°E for the period of this study.

In addition to the wind stress fields, the daily SAM Index, obtained from the National Oceanic and Atmospheric Administration Climate Prediction Center (www.cpc.ncep.noaa.gov), is used in this work as a proxy for the large-scale atmospheric circulation in the Southern Ocean. This index is based on the NCEP-NCAR reanalysis and is defined as the projection of the 700 mb height anomalies poleward of 20°S onto the leading mode of Empirical Orthogonal Function analysis of monthly mean 700 mb height during the 1979–2000 period.

### 2.5. Sea Surface Height Observations

Satellite altimetry provides weekly sea surface height (SSH) observations that can be used to investigate the geostrophic component of the ocean dynamics [*Le Traon and Dibarboure*, 1999]. In addition to the XBT-derived snapshots south of Africa, SSH data is used in this study to assess the SAF and APF variability through (1) the definition of frontal positions and (2) baroclinic transports for the period between 1993 and 2010. SSH anomaly (SSHA) data is obtained from the AVISO delayed-time/reference database (available at http://www.aviso.oceanobs.com). This gridded product corresponds to the combination of measurements of multiple altimeters, is homogeneous in time, and is available at weekly intervals with a spatial resolution of 1/4° [*Le Traon et al*., 1998]. SSHA observations are added to a mean dynamic topography [*Rio et al*., 2011; referred to as CNES-CLS09] to produce fields of Absolute Dynamic Topography (ADT). The ADT based on the CNES-CLS09 global climatology provides a refined ACC structure [*Rio et al*., 2011], which is used in this work to investigate the SAF and APF variability.

## 3. Methods

### 3.1. Frontal Regions

A frontal region is usually defined in terms of water mass properties. The ACC fronts are defined in this study based on the subsurface potential temperature ($\theta$) structure using one traditional method [*Orsi et al*., 1995]: (a) the STF, which marks a sharp transition from the warmer ($\theta_{100m} > 12°C$) Subtropical Water to the colder ($\theta_{100m} < 10°C$) Subantartic Surface Water (SASW) and has been located at ~40°S along AX25; (b) the SAF, which is defined by the temperature change ($\theta_{400m} > 4$–$5°C$) associated with the northern boundary of the transitional zone between the SASW and the Antarctic Surface Water (AASW) and has been located at ~48°S; (c) the APF that is defined based on the temperature maximum ($\theta_{0\text{–}200\ m} < 2°C$), from south to north, associated with the sinking AASW, and has been located at ~50°S; (d) the sACCf, which is defined based on the temperature minimum ($\theta_{<500\ m} < 1.8°C$) associated with the Upper Circumpolar Deep Water (UCDW) and has been located at ~52°S; and (e) the SBdy that is defined based on the temperature minimum ($\theta_{\sim 200\ m} > 1.5°C$) associated with the southern extent of the UCDW and has been located at ~56°S. The frontal locations described above were estimated based on historical hydrographic profiles in the Southern Ocean during 1930–1990 [*Orsi et al*., 1995]. In this study, the focus on temporal variability is limited to the SAF and the APF.

The definitions above are based on the subsurface potential temperature structure [*Orsi et al*., 1995]. Altimetry-derived methods also provide an accurate definition of the mean ACC fronts consistent with the subsurface temperature method [*Swart et al*., 2010], which justifies the use of altimetry observations here to monitor the location of the SAF and of the APF since 1993 and to fill in the seasonal gaps not sampled by the occupations of AX25 after 2004. Several studies have applied altimetry observations to investigate the variability of the ACC fronts at various locations [*Sallee et al*., 2008; *Sokolov and Rintoul*, 2007, 2009a, 2009b; *Swart et al*., 2010; *Billany et al*., 2010], using one specific dynamic height value to determine the frontal locations. However, it has been recognized that the frontal locations as defined by this methodology may differ from the position of the actual maximum dynamic height gradient [*Sallee et al*., 2008]. In fact, previous results in the region of study [*Billany et al*., 2010] showed that the SSH-contour definition provided a frontal location that coincided with the maximum SSH-gradient only during 25% of the time for the SAF, and during 35% of the time for the APF. Therefore, using one specific dynamic height value to determine the frontal location may provide underestimated values of variability. To avoid this issue, the location of the SAF and APF is defined here based on the ADT gradient within the known latitudinal range of these fronts. Several peaks in the ADT gradient within the frontal region may occur due to the multiple branch structure of the ACC fronts [*Sokolov and Rintoul*, 2007]. The axial position of each front is defined here based on the maximum ADT gradient (or the most energetic branch) within the predetermined frontal region [*Swart et al*., 2008, 2010; *Billany et al*., 2010].

In order to compute the transport of SAF and APF, the frontal region needs to be determined. The multiple branch structure of the SAF and APF [*Sokolov and Rintoul*, 2007] makes the definition of the frontal region a difficult task. This is because assigning each branch to a specific front can be subjective. In addition, previous studies recognized the SAF and APF multibranch structure along AX25 [*Gladyshev et al*., 2008; *Swart et al*., 2008]. Therefore, a dynamic definition is adopted here, which is consistent with the altimetry-based definition for the frontal location. From north to south, the boundaries of the frontal regions are defined as follows: (i) Northern SAF boundary – lowest positive ADT gradient to the north of the SAF location; (ii) SAF-APF boundary—lowest positive ADT gradient to the south of the SAF and to the north of the APF, which provides a unique latitude when there is no westward flow between the location of these fronts; and (iii) Southern APF boundary—lowest positive ADT gradient around 52°S. The 52°S value is used because the sACCf experiences very small temporal variability south of this latitude [*Swart et al*., 2008; *Billany et al*., 2010]. Because of the spatial resolution of the gridded altimetry data used here, the minimum frontal width that can be determined using this definition is 50 km. Also, this definition for the frontal domain is independent of the frontal location and ensures that the individual transport contribution from each branch is accounted for in the total frontal transport.

### 3.2. Baroclinic Transports

For each XBT realization, the cumulative transport along AX25 is estimated using a standard methodology [*Baringer and Garzoli*, 2007], where: (1) salinity is estimated using historical T-S relationships from the annual climatology [World Ocean Atlas 2001-WOA01, *Stephens et al*., 2002]; (2) temperature observations from 800 m to the bottom are obtained by interpolating the WOA01 to the location of each profile, generating an annual mean climatology for the deep ocean; (3) geostrophic velocities are determined using the dynamic method referenced to the bottom from the 2 min gridded bathymetry [*Smith and Sandwell*, 1997], and (4) cumulative transports are calculated by integrating the velocity fields along AX25, starting from the southernmost XBT site (~70°S). Since some of the XBT realizations did not cover the entire transect, for these transects the cumulative transports are completed between ~70°S and its southernmost site using the mean transport of 10 transects that covered the full length of AX25.

### 3.3. Wavelet Analysis

Wavelet transform (WT) [*Grinsted et al*., 2004] is applied here to analyze the temporal variability of the parameters considered in this study. The wavelet analysis has been consistently applied in meteorology and oceanography to highlight significant modes of variability [*Weng and Lau*, 1994; *Foufoula-Georgiou and Kumar*, 1994; *Goni et al*., 2011]. This analysis decomposes the signal into dominant modes as a function of time, providing information about temporal changes in the spectral characteristics of the time series.

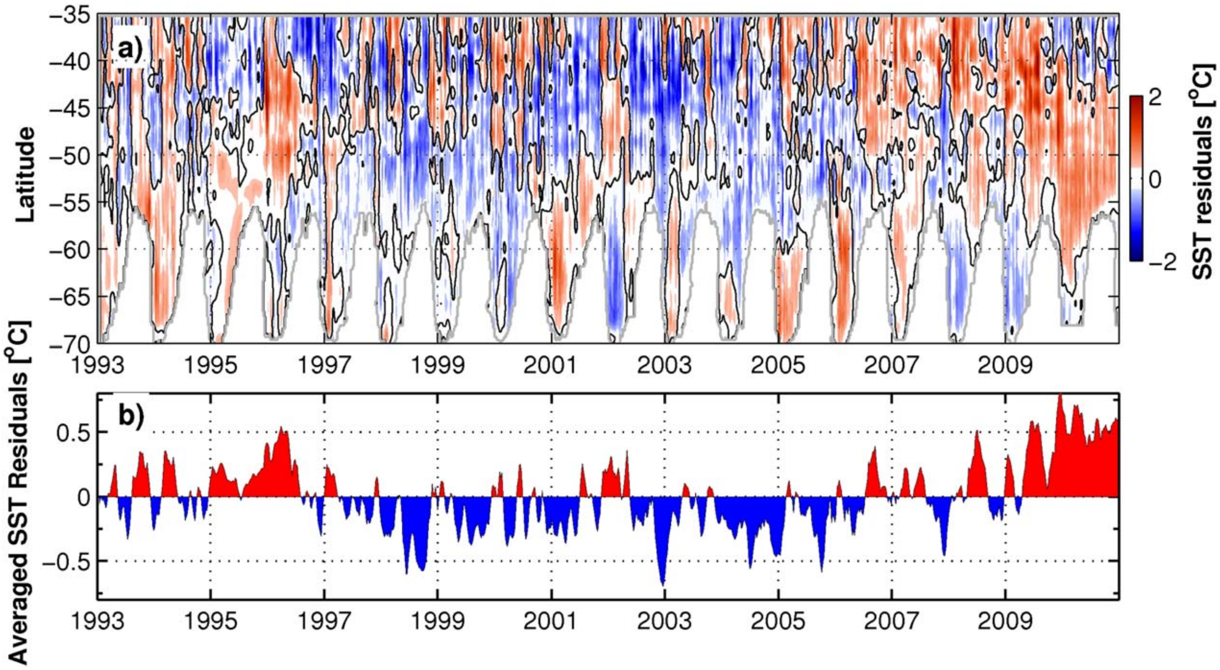


**Figure 2.** (a) Satellite-derived SST residuals along AX25. White areas represent data gaps due to sea-ice. (b) Meridionally averaged SST residuals in the ACC region between 45°S and 55°S.

### 3.4. Statistical Analysis

All analyses performed in this work are statistically evaluated at a 95% significance level. A double tail *t* test is used to assess the significance of the correlation coefficients. For filtered time series, the degrees-of-freedom is calculated by dividing the length of the time series by the length of the low-pass filter window.

## 4. Results

This section is organized as follows: sections 4.1 and 4.2 assess the variability of the SST and of the subsurface temperature along AX25, respectively, which are important because the variability of the thermal structure of the ACC may be linked to the SAF and APF variability (e.g., due to frontal motions); section 4.3 evaluates the transports across AX25, which are used to calculate the SAF and APF transports; sections 4.4 and 4.5 describe the variability of the frontal motions/transports for the SAF and for the APF, respectively, and investigate their link with the variability of the thermal structure; and section 4.6 assesses the atmospheric variability and its links with the SAF and APF variability.

### 4.1. Sea Surface Temperature Variability

The analysis of the SST variability focuses on the meridional subset between 45°S and 55°S, which is considered as representative of the core of the ACC. This latitude range is chosen to avoid the influence of SST anomalies induced by the Agulhas Rings, as will be discussed in section 4.2. The SST seasonal cycle along AX25 (not shown here) has an amplitude of $\sim$2°C in the ACC region between 45°S and 55°S, with a maximum temperature of 4.6°C during March and a minimum of 2.8°C during September. The satellite-derived SST residuals (seasonal cycle removed) range between $-$1.9°C and 2.4°C along the transect (Figure 2a). In the ACC region, mostly cold residuals are observed between 1997 and 2008 (Figure 2b), while warm residuals lasting longer than 4 months are observed in 1994–1996, 2001–2002, 2006, 2008, and 2009–2010. These warm events may last as long as 21 months, reaching up to 2°C, and are connected with warm residuals located to the north of 45°S. After 2007, two warm events are identified (Figure 2a): (a) one starting in the summer of 2008 north of 45°S, reaching 55°S in the late-fall/early-winter of that same year; and (b) a second event starting in the summer of 2009. This latter event was more persistent, with the warm residuals remaining between 45°S and 55°S for more than 21 months. These two events are highlighted because

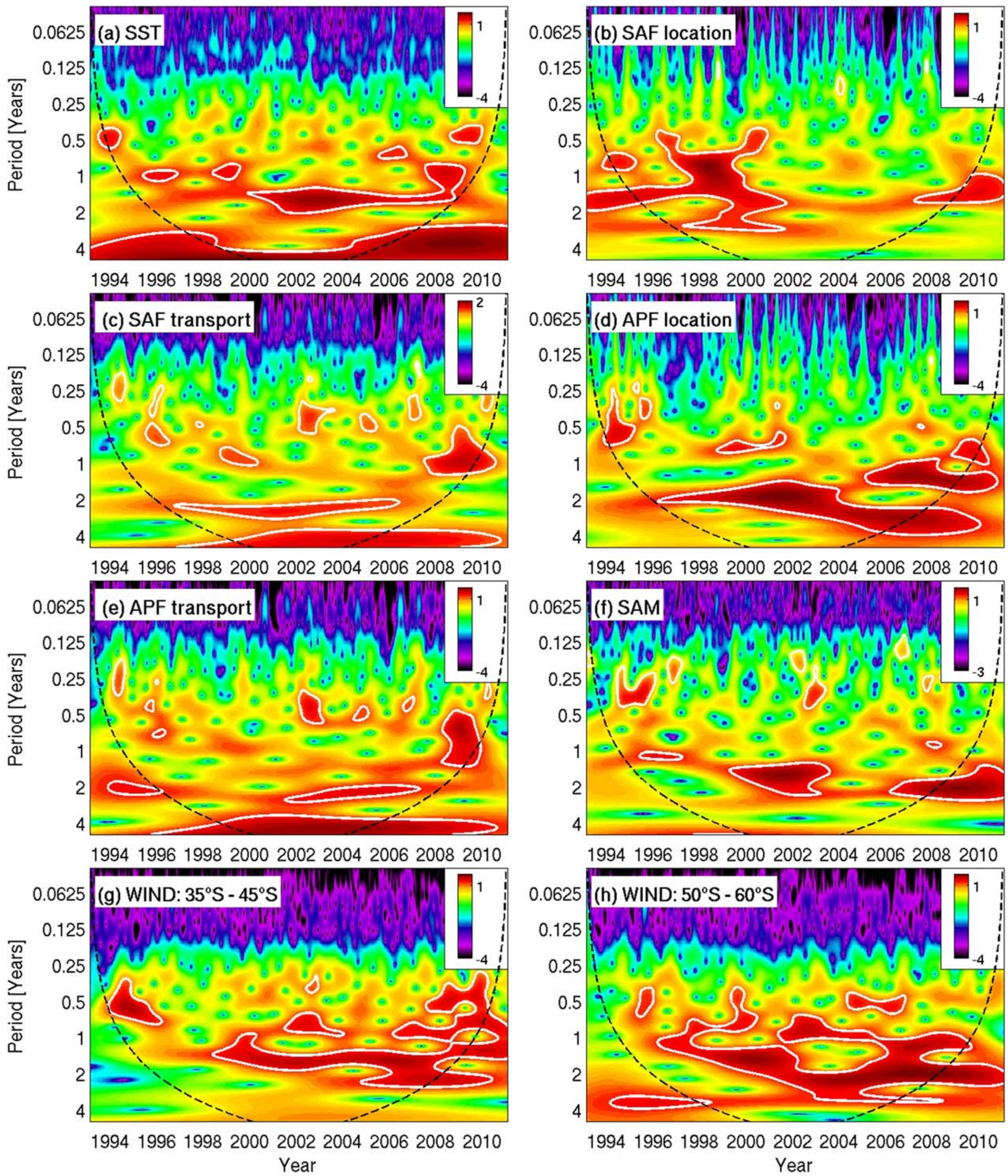


**Figure 3.** Wavelet Spectrum Density of: (a) SST within 45°S–55°S along AX25, (b) SAF latitude, (c) SAF transport, (d) APF latitude, (e) APF transport, (f) SAM, (g) wind stress within 35°S–45°S along AX25, and (h) wind stress within 50°S–60°S. The solid white contours represent the peak-based significance levels, computed at 95%. The dashed curve indicates the cone of influence. Power and units are the square of the parameter unit (e.g., temperature—°C$^2$).

there are in situ observations during those periods, which are used to assess the variability of the subsurface layers.

The variability of the SST residuals averaged between 45°S and 55°S (Figure 2b) exhibits significant periodicity throughout the record (Figure 3a): (1) ~1.5 year period variance between 2001 and 2009; (2) semiannual variance centered in 1994, 2006, and 2009; and (3) annual variance centered in 1996, 1999, and

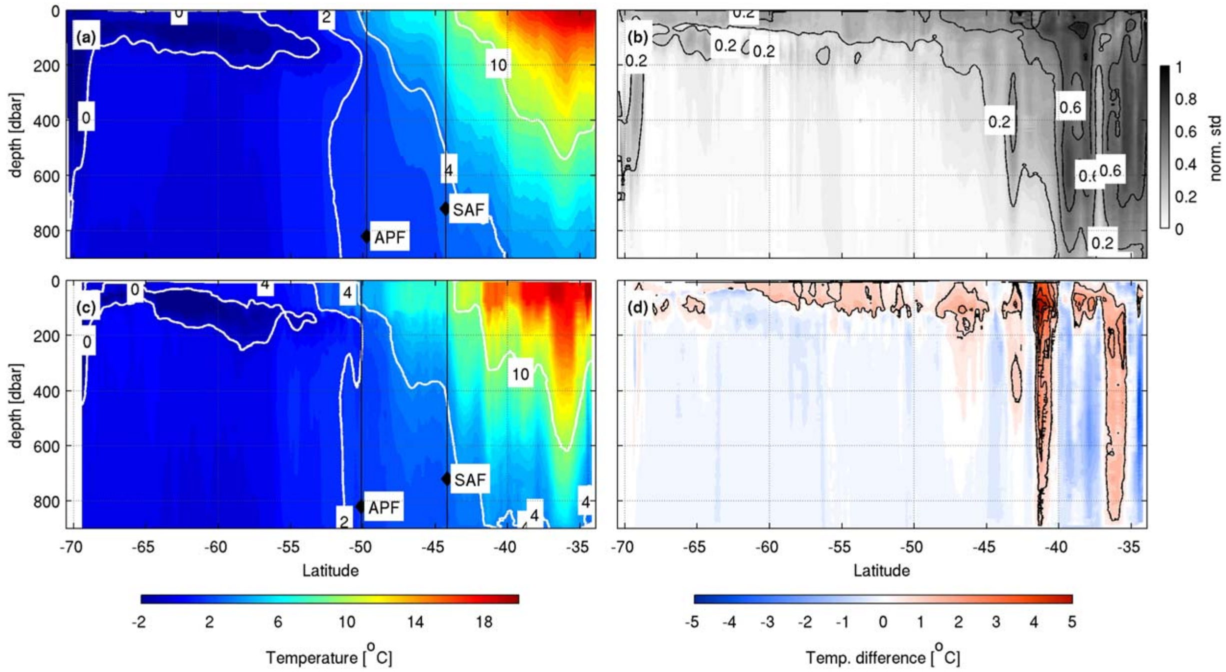


**Figure 4.** (a) Section of mean temperature and of (b) normalized standard deviation of the 16 AX25 XBT realizations; (c) temperature section for February 2010, and (d) difference between February 2010 temperature section and the mean temperature. The 0, 2, 4, and 10°C isotherms (white contours) are highlighted in Figures 4a and 4c, while positive anomalies contours of 1–4°C (black lines) are shown in Figure 4d.

2008–2009. These variances are located within the cone of influence, which reflects an actual change in the spectral characteristics of the time series. Additionally, the WT suggests the existence of variability with periods larger than 4 years. However, most of this power is out of the cone of influence and subject to edge effects. Therefore, longer records are needed to assess the validity of the variability with periods of 4 years and longer.

### 4.2. Subsurface Temperature Variability

Along AX25, higher subsurface temperature variability (Figure 4b) is concentrated north of 45°S because of the Agulhas Retroflection and Rings that are shed into the region as well as in the upper 100 m south of 45°S. As an example, the February 2010 transect (Figures 4c–4d) shows temperature differences, with respect to the average thermal structure, as large as 2°C (5°C) in the upper 100 m (between 0 and 900 m) between 45°S and 55°S (north of 45°S). In addition, observations from Argo and CTD profiles further indicate that the deep layer (900–2000 m) between 45°S and 55°S is subject to small temperature anomalies throughout the year (not shown). This shows that the SAF and APF region is subject to small temperature variations that are mostly confined to the upper-layer.

Seasonal averages based on the in situ temperature profiles are computed by averaging the observations in blocks of 3 months. For example, the summer averages are computed grouping the data collected during January, February, and March. The residuals are calculated as the difference between the seasonal averages for that year and the seasonal mean during 2002–2010. The Hovmöller diagram (Figure 5) indicates that between 45°S and 55°S the residuals can be as large as 1.5°C in the upper-layer (0–100 m), and are close to 0°C in the lower layer (100–900 m). North of 45°S, residuals range between −2°C and 2°C for both layers, which may be due to the influence of Agulhas Rings. Starting in 2008, residuals larger than 0.5°C in the upper-layer between 45°S and 55°S are consistent with the warm events previously described for the SST. Positive residuals of this magnitude are not observed in the intermediate layer for the same period and region, indicating that such anomalies are confined to the first 100 m of the water column.

### 4.3. The ACC Transport

The average XBT-derived baroclinic transport across AX25 is 132 ± 9 Sv. The mean cumulative transport (Figure 6) integrated from south to north (i) starts at 0 Sv at 70°S (ice shelf of Antarctica), (ii) decreases down to

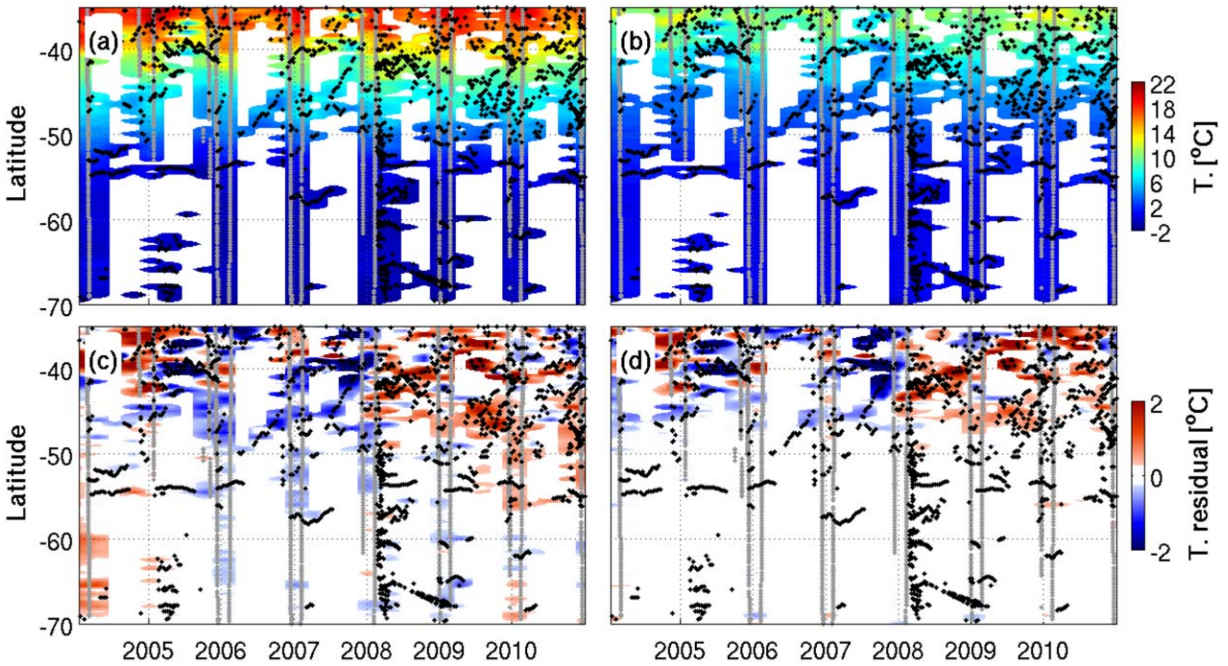


**Figure 5.** Seasonally averaged temperature and its corresponding residual values along AX25 based on Argo (black dots) and XBT profiles (gray dots) for the upper-layer (0–100 m, Figures 5a–5c), and intermediate-layer (100–800 m, Figures 5b–5d). White areas mark periods of missing data.

$\sim -20$ Sv at 60°S due to the westward flowing branch of the Weddell Gyre, located between approximately 70°S–63°S, (iii) increases up to $\sim$150 Sv at 37°S because of the dominant ACC flow to the east, and (iv) decreases down to $\sim$130 Sv at 35°S due to the westward flow associated with the passing of Agulhas Rings in the region. The cumulative transports by single AX25 realizations emphasize the high variability induced by the Agulhas Rings north of 45°S. The average eastward transport between 37°S and 40°S is due to the southern edge of anticyclonic Agulhas Rings. Between 37°S and 56°S, localized maxima in the cumulative transport meridional gradient indicate the presence of the ACC fronts as follows: (1) the gradient of 22 Sv/° latitude at 56°S corresponds to the SBdy; (2) the gradient of 17 Sv/° latitude at 53°S corresponds to the sACCf; (3) gradients larger than 14 Sv/° latitude between 47 and 50°S correspond to the multibranch structure of the APF; (4) gradients larger than 17 Sv/° latitude between 44 and 46°S correspond to the multibranch structure of the SAF; and (5) the gradient of 9 Sv/° latitude at 38°S corresponds to the STF. Although the signal of the latter front is evident in the meridional gradient of the average cumulative transport, the temporal and spatial continuity of the STF is still a matter of discussion [*Belkin and Gordon*, 1996; *Boebel et al.*, 2003], and in this region the STF is often considered to be a product of the frequent presence of eddies [*Lutjeharms*, 1988; *Lutjeharms and Valentine*, 1984; *Belkin and Gordon*, 1996; *Dencausse et al.*, 2011]. Although this result indicates that it is possible to identify the ACC fronts through meridional gradients of the cumulative transport, in this study these fronts are located during 1993–2010 using a different methodology (section 3.1), and the results will be presented for the SAF (section 4.4)

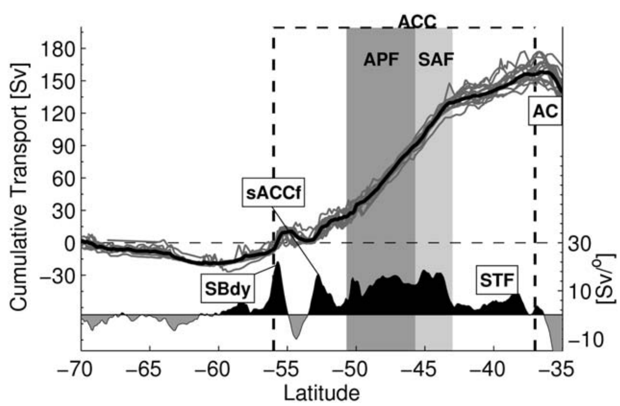


**Figure 6.** Total transport for each of the 16 AX25 realizations (gray lines) and their average (black line). The total transport per degree of latitude is shown with positive (black) and negative (gray) shading. The mean locations of the ACC fronts (STF, SAF, APF, sACCf, and SBdy) and of the Agulhas Current are shown.

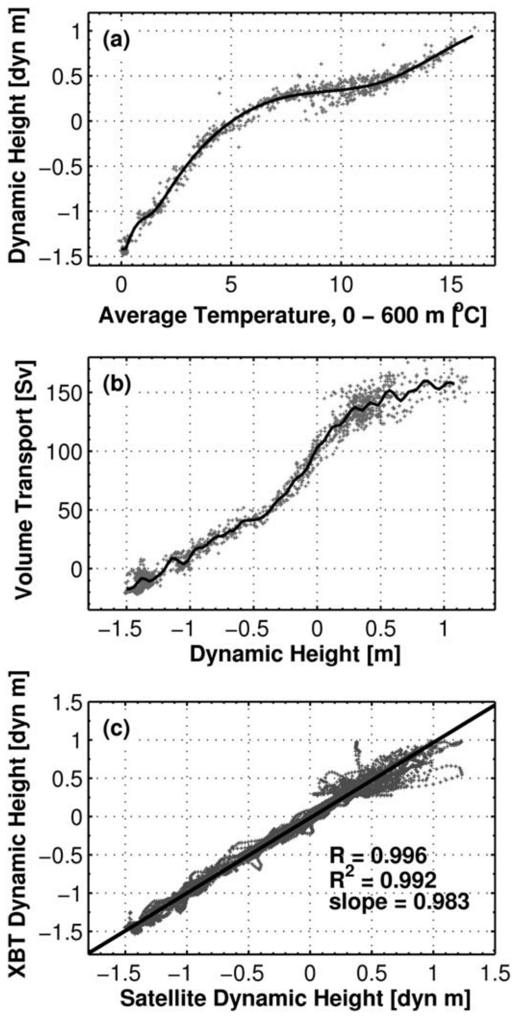


**Figure 7.** Empirical relationships between (a) Argo and CTD absolute dynamic height and the average temperature between 0 and 600 m; (b) cumulative transport across AX25 and the dynamic height estimated from XBT data; (c) Regression between the dynamic height estimated from XBT data and the satellite-derived dynamic height. Black lines denote the spline (Figures 7a and 7b) and linear (Figure 7c) fit for these relationships.

and APF (section 4.5) separately. In addition, the average ACC baroclinic transport, computed here between the STF and SBdy, is 154 ± 6 Sv. This value falls between previous estimates of 162 Sv [*Whitworth and Nowlin*, 1987] and 147 Sv [*Legeais et al*., 2005] south of Africa.

Four steps are used here to compute the weekly cumulative transport estimates from altimetry observations during 1993–2010 [*Swart et al*., 2008]:

1. A spline fit between the average temperature at 0–600 m $\left(\overline{T_{0-600}}\right)$ and the absolute dynamic height (SF1, Figure 7a) is applied based on the Argo and CTD T-S profiles;

2. The XBT-derived $\left(\overline{T_{0-600}}\right)$ is used to compute the absolute dynamic height for the AX25 realizations using SF1;

3. A spline fit is applied between the XBT-derived absolute dynamic height and the XBT-derived cumulative transport (SF2, Figure 7b); and

4. The altimetry-derived cumulative transport is estimated using SF2, assuming that the ADT is equivalent to the XBT-derived absolute dynamic height (Figure 7c).

The altimetry-derived cumulative transports, which will be used to assess the transport variability of the SAF (section 4.4) and of the APF (section 4.5), are compared here with the XBT-derived cumulative transports for the AX25 realizations (Figure 8). The differences between the estimates from these two platforms are less than 5 Sv in the ACC region and can be as high as 15 Sv to the north of 45°S. These higher differences may be due to the facts that (1) there is a reduction of the spline "tightness" toward the northern ends of the section and (2) the empirical relationship applied may partly remove the variability related to transient features north of 45°S (e.g., Agulhas Rings). However, it is unlikely that this issue affects the transport computations for the SAF and APF, because these fronts are usually located to the south of the region influenced by Agulhas Rings and other forms of STF variability [*Swart et al*., 2008; *Billany et al*., 2010].

### 4.4. The SAF Location and Transports

The average location of the SAF during 1993–2010 (Figure 9a) is 44.5 ± 0.8°S, which falls within the range of previous estimates for the location of this front south of Africa. For example, hydrographic estimates of the average SAF location reported values of 44.6°S [*Swart et al*., 2008] and of 45.7°S [*Orsi et al*., 1995], while average altimetry-based locations were 45.3°S [*Billany et al*., 2010] and 44.3°S [*Swart et al*., 2010].

The altimetry-derived SAF location is placed here at the location of the maximum geostrophic velocity, and it differs by 13 ± 47 km from the XBT-derived location to the north. This difference implies that both

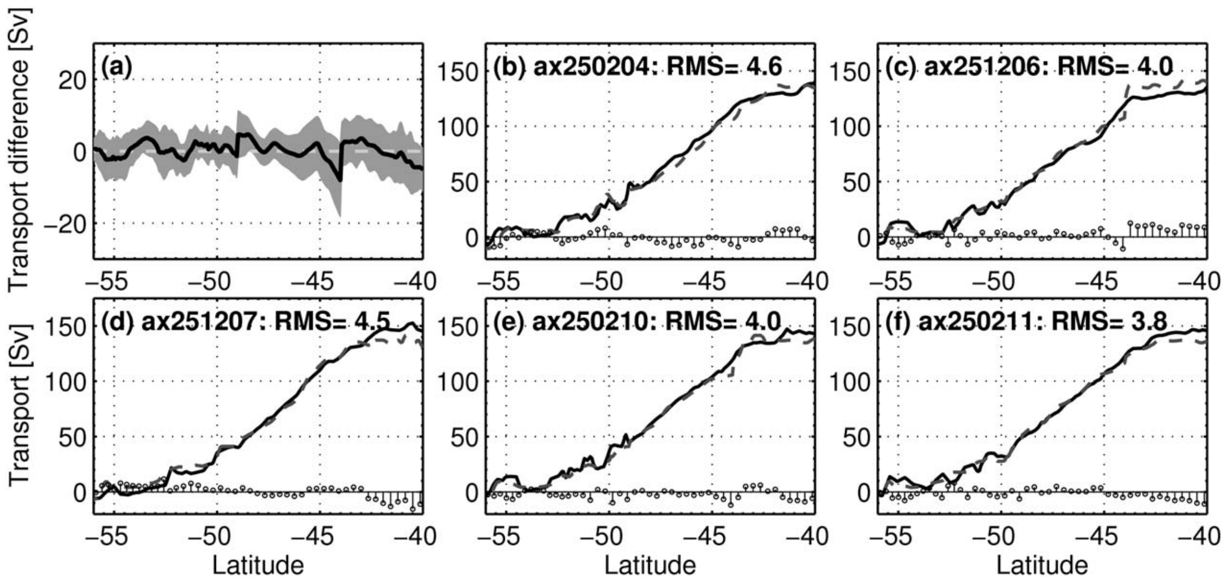


**Figure 8.** (a) Average (black line) and standard deviation (gray shading) of the difference between the satellite-based transport, using the proxy method in Figure 7b, and the XBT-derived transport. Figures 8b–8f exhibit the satellite-derived (gray dashed line) and the XBT-derived (black line) cumulative transports corresponding to the AX25 realizations on February 2004, December 2006, December 2007, February 2010, and February 2011, respectively. The RMS difference between each station pair of XBT-derived and satellite-derived transports is exhibited along the *x* axis.

methods provide statistically the same mean SAF location, and may be because the subsurface expression of a front is not always found directly beneath its surface expression [*Lutjeharms*, 1985]. No seasonal cycle is found in the SAF location south of Africa during 1993–2010 (not shown here), which is in agreement with previous observations [*Billany et al*., 2010]. The time scale of SAF meridional shift varies with time, experiencing semiannual variability during 1995 and 1997–2001, whereas during 1993–2002 and 2004–2010 it fluctuates with a period of $\sim$ 2 years (Figure 4b).

The SAF location ranged between 43°S and 46.5°S, which is a larger range than the $\sim$2° latitude range reported when the SAF was defined using a specific dynamic height contour [*Billany et al*., 2010; *Swart and Speich*, 2010]. This indicates that the location of one specific contour of dynamic height is less variable than the location of the maximum gradient. The higher variability of the maximum gradient location may be due to the fact that the SAF crosses the Mid-Ocean Ridge (Figure 1) upstream from reaching AX25, which may influence its dynamics through the generation of baroclinic instabilities [*Thompson and Richards*, 2011]. Strong meandering is observed between 6°W and 6°E (not shown here), where the topography is relatively flat, indicating the growth of these instabilities. Therefore, it is hypothesized here that the use of a fixed contour to track the fronts in regions of varying bottom topography may lead to an underestimation of the variability of frontal motions. However, further studies are needed to confirm this.

The SAF boundaries are determined using local minimum geostrophic velocities (Figure 9a). The average location of the SAF boundaries compares reasonably well with the SAF boundaries defined using fixed dynamic height values [*Swart et al*., 2008]. However, the definition of the SAF based on low geostrophic velocities has the advantage of ensuring that even small features are fully included in the frontal region. The SAF boundaries are used here to compute the transports associated with this front during altimetry period 1993–2010 (section 4.3). The SAF transport is therefore defined as the cumulative transport between the southern and northern boundary. The average SAF transport during 1993–2010 is 64.6 ± 13.1 Sv, which is in agreement with the previously reported full water column transport of 61 Sv [*Legeais et al*., 2005] obtained from hydrographic surveys during 1984–1992. An altimetry-based computation of the SAF transport has also been used in a shorter record and referenced to 2500 db [*Swart et al*., 2008], which estimated an average value of 33.3 ± 3.1 Sv. However, this value is not comparable to the SAF transport computed here because of the different reference levels (bottom-referenced is used here). The relative SAF contribution to the ACC transport calculated here ($\sim$42%) is the

  

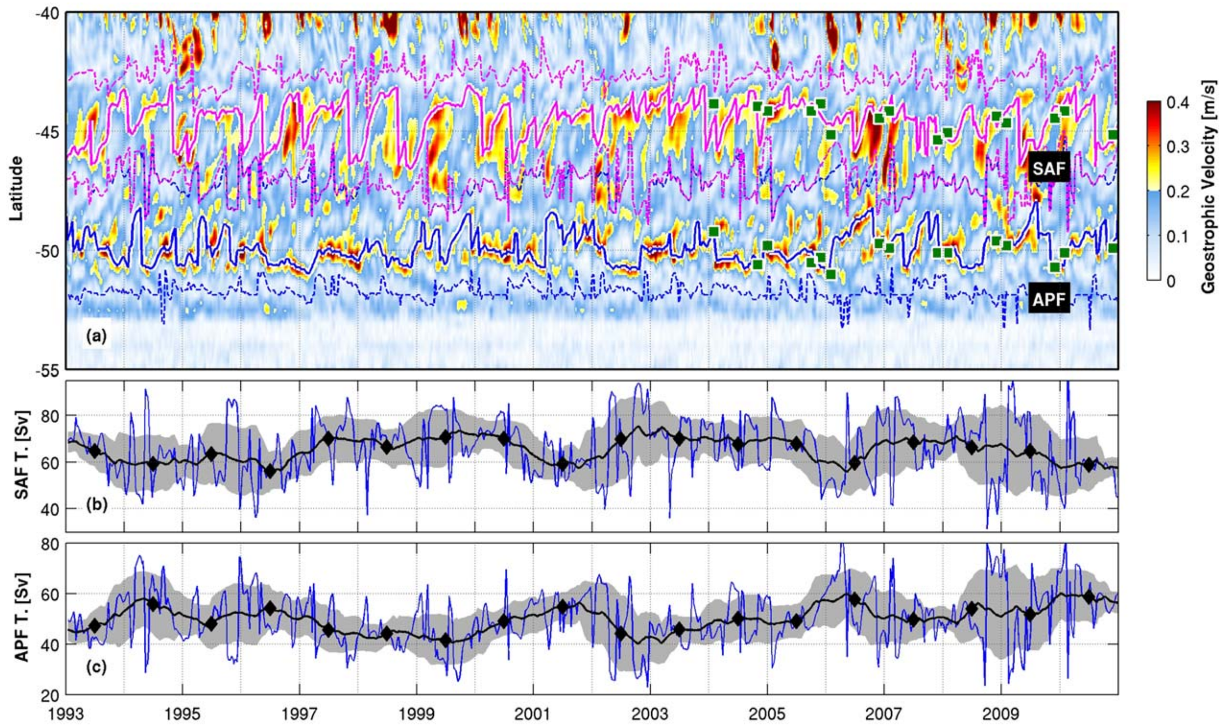


**Figure 9.** (a) Time series for the location of the SAF (solid magenta line) and APF (solid blue line) based on the altimetry and on XBT data (green squares) overlaid on the altimetry-derived geostrophic velocities (in m s$^{-1}$). The SAF and APF frontal boundaries are also displayed (dashed lines). (b) Transport time series for the SAF (blue line), showing the 1 year running mean (black line) and standard deviation (gray shaded area), and the annual means (black diamonds). (c) Same as Figure 9b but for the APF.

same as the value reported by *Legeais et al*. [2005] and close to the value reported by *Swart et al*. [2008] (39.2 ± 2.5%).

The SAF transport exhibits year-to-year variability during 1993–2010 (Figure 9b). The annual averages range from 56 Sv to 71 Sv. Significant annual periodicity is not always observed, as it appears only during 2008–2009 (Figure 3c). The SAF transport also varies with periods longer than a year during most of the record. Small but significant positive correlations between the SAF location and the SAF transport (Figure 10a) are found, with the SAF location leading by approximately 5 weeks, indicating that a northward displacement of the SAF is followed by intensification in the SAF transport. On the other hand, the significant negative correlations between the SAF location and the averaged SST residuals between 45°S and 55°S (Figure 10b) indicate that a southward displacement of the SAF is followed by a warming in the ACC after approximately 1 year (53 weeks). The negative correlation between the SAF location and the upper-layer temperature may be due to advection of warmer surface waters during the southward displacement of the SAF. This result is in agreement with observation-based [*Gille*, 2008; *Boning et al*., 2008; *Sprintall*, 2008] and modeling-derived studies [*Hall and Visbeck*, 2002; *Alory et al*., 2007; *Fyfe et al*., 2007], which suggested that the warming trend in the ACC is due to the southward displacement of the ACC fronts. The SAF transport also has significant negative correlations with the SST (Figure 10c) centered at zero lag, which indicates that a lower SAF transport coincides with warmer SST between 45°S and 55°S. These two time series are better correlated at lower frequencies. The slope of the linear regression between them at zero lag and with a one year low-pass filter indicates that a warm anomaly of 1°C in the upper-layer of the ACC is associated with a decrease of 13 Sv in the SAF transport. The correlations evaluated here present a link between the variability of the SAF location, the SAF transport, and the upper-layer temperature in the ACC. The potential forcing mechanism linking these parameters will be discussed in section 5.

### 4.5. The APF Location and Transports

The temporal variability of the APF is evaluated here and then compared to changes in the upper-layer temperature. The average location of the APF during 1993–2010 is 49.9 ± 0.7°S, which is consistent with

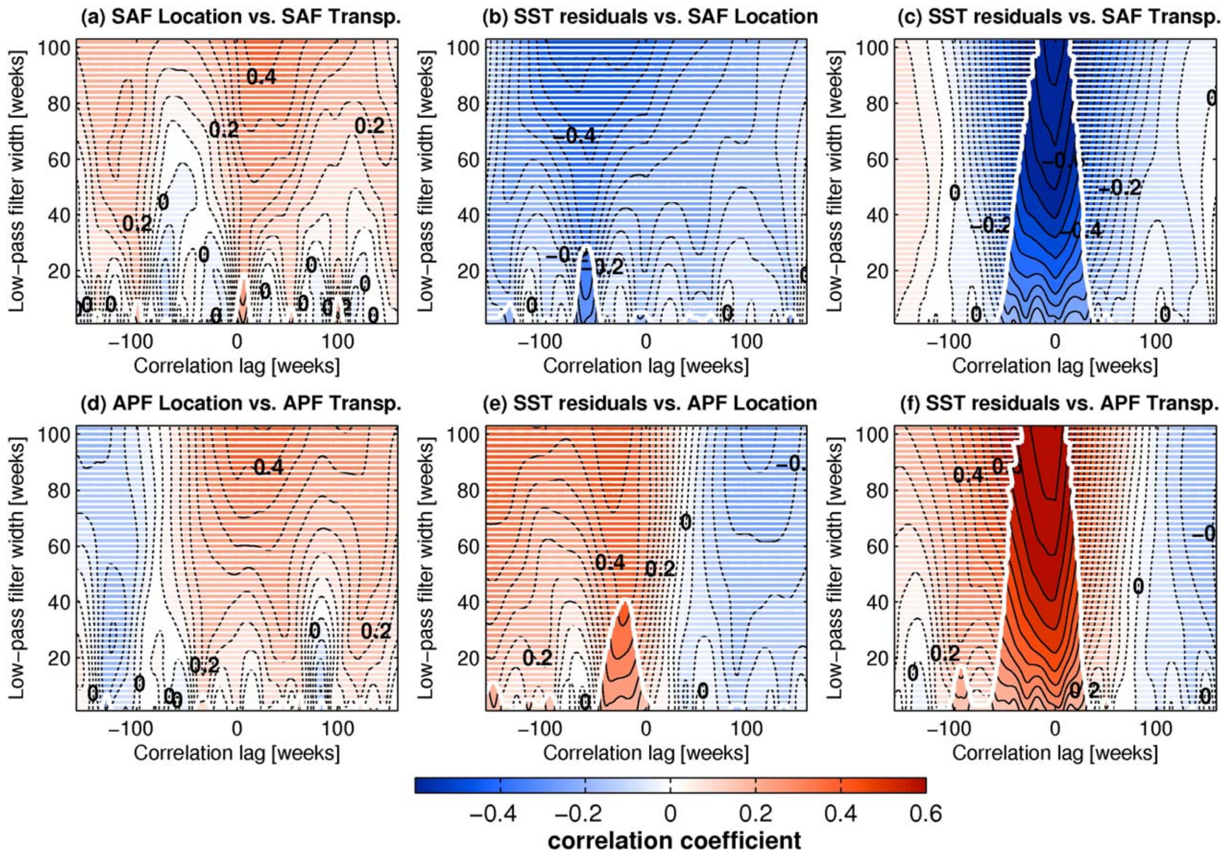


**Figure 10.** Correlation coefficients between: (a) the SAF location and the SAF transport; (b) the SST residuals between 45°S and 55°S, and the SAF location; (c) the SST residuals between 45°S and 55°S, and the SAF transport; (d) the APF location and the APF transport; (e) the SST residuals between 45°S and 55°S, and the APF location; (f) the SST residuals between 45°S and 55°S, and the APF transport. Each diagram shows the correlation coefficient as a function of the lag in weeks between the two time series (*x* axis) and of the low-pass filter width applied (*y* axis). Nonsignificant correlations ($p > 0.05$) are illustrated by the white dashing.

previous estimates. Previous hydrographic estimates reported an average location of 49.6°S [*Orsi et al*., 1995] and of 50.4°S [*Swart et al*., 2008], while altimetry-based estimates reported an average location of 50.0°S [*Billany et al*., 2010; *Swart et al*., 2010]. The altimetry-derived APF location is located at the position of the maximum geostrophic velocity (Figure 9a), and is on average slightly to the north of the XBT-derived location by 5 ± 24 km. Similarly to the SAF, both the altimetry-derived and the XBT-derived methods provide the same statistical mean APF location.

The APF location ranges between 48°S and 51.4°S and exhibits no seasonal cycle during 1993–2010 (not shown), which is consistent with previous observations [*Billany et al*., 2010]. The APF location (standard deviation = 0.7° latitude) exhibits a meandering behavior that is less variable than the SAF location (standard deviation = 0.8° latitude). This is possibly because the APF may be partially steered by the topography after crossing the Mid-Ocean Ridge (Figure 1), while the SAF may develop meanders due to baroclinic instability [*Thompson and Richards*, 2011] in the absence of topographic steering. During 1993–2010, the EKE (Figure 1b) signal associated with the APF is parallel to topographic features between 6°W and 6°E, while the signal associated with the SAF is not related to any topographic features. Although less variable, the APF location also exhibits significant periods longer than one year (Figure 3d), which is similar to the computed periodicity of the SAF location. The location of the APF has periodicity of ~2 years during 1996–2004, which changes into both a longer (~3 years) and shorter (~1.5 years) period after 2004. Semiannual periodicity in the APF location is only observed during 1994–1996 and 1998–2002.

Similar to the SAF, the APF boundaries are determined using local minimum geostrophic velocity. These frontal boundaries also compare reasonably with the boundaries defined by a fixed dynamic height as in a previous study [*Swart et al*., 2008]. The APF boundaries are used here to compute the baroclinic transport of this front during 1993–2010, using the same methodology to compute the SAF transports (section 4.4). The mean APF baroclinic transport computed here is 51.0 ± 11.8 Sv (Figure 9c), which differs by less than one standard deviation from previous computations of 41 Sv [*Legeais et al*., 2005] and 49 Sv [*Gladyshev et al*., 2008]. The APF transport corresponds to ~33% of the total ACC baroclinic transport computed here (section 4.3), which is smaller than the ~42% transport contribution from the SAF transport. A similar composition of the ACC transport has been previously observed in a full water column computation [*Legeais et al*., 2005], in which the SAF and APF transports corresponded to 42% and 28% of the total ACC transport, respectively. A different composition of the ACC transport was observed when the SAF and APF transports were referenced to 2500 db [*Swart et al*., 2008], in which the SAF and APF transports corresponded to 39.2 ± 2.5% and 48.4 ± 3.3% of the total ACC transport, respectively. Although these differences may be partially due to the specific methodology adopted to define the frontal region (e.g., one method may include more frontal branches than the other), the deep component of the transports could also induce such differences. This is especially true along AX25, because the SAF region is considerably deeper (average depth = 4250 m) than the APF region (average depth = 3400 m).

The dominant variability of the APF transport has a period of 2 years (2001–2007, Figure 3e). The annual means of the APF transport exhibit large year-to-year variability (Figure 9c). The evaluation of the APF and SAF transport time series indicates that an increase in the value of the APF transport corresponds to a decrease in the SAF transport, and vice versa. For example, the largest annual mean APF transport was 58 Sv in 2006 and the smallest was 42 Sv in 1999, while in 2006 the SAF had a low transport of 58 Sv and in 1999 it had the highest annual average of 71 Sv. The negative relationship between the SAF and the APF transport is evident throughout the record. The linear regression coefficient between the two frontal transports at time-scales longer than annual is −0.8. This relationship will be further addressed in section 5.

Different from the SAF, no statistically significant correlations are found between the APF location and the APF transport (Figure 10d). The APF location also exhibits no significant correlations with the averaged SST residuals between 45°S and 55°S (Figure 10e). On the other hand, the APF transport exhibits significant positive correlations with the SST residuals centered at zero lag (Figure 10f), with higher correlations obtained at frequencies lower than 1 year. These results show that a higher APF transport coincides with a warmer upper-layer between 45°S and 55°S. This is similar to the relationship observed between the SAF transport and the SST residuals, however with a different sign. Therefore, the correlations evaluated here present a link between the variability of the temperature in the upper-layer of the ACC and the variability of the APF and SAF transports. Warm SST residuals between 45°S and 55°S are associated with a stronger APF transport but weaker SAF transport, which suggests an integrated response of the ocean to external forcing. Discussions in section 5 will further address these relationships.

### 4.6. Atmospheric Variability

The relationship of the atmospheric forcing with the upper-ocean temperature and frontal (SAF and APF) transports is investigated here. The average zonal wind stress for the ACC region between 45°S and 55°S along AX25 during the period 1993–2010 is 0.13 ± 0.06 N/m$^2$, and it has a seasonal cycle (not shown here) with an amplitude of 0.07 N/m$^2$ between 35°S and 45°S, and of 0.05 N/m$^2$ between 50°S and 60°S. These two meridional subsets are highlighted because their variability is associated with meridional changes in the structure of the westerlies, as will be seen next. Along AX25, the axial position of the westerlies is located at ~49°S, while the westerlies/easterlies reversal is located at ~65.5°S.

The SAM is an important component of the wind stress variability in the Southern Ocean [*Marshall*, 2003]. During the study period there is no statistically significant trend for the SAM index (Figure 11a), which suggests the stabilization of the SAM after a rising trend during 1958–2000 [*Marshall*, 2003]. The large-scale pattern during a positive phase of the SAM index is indicative of the southward displacement of the westerlies [*Gupta and England*, 2006]. Observations analyzed here show that structural changes in the local wind stress are linked to the SAM. During extreme negative SAM (5% smaller, $<-1.6$), the axial position of the westerlies is located at ~44°S (Figure 11b), while during extreme positive SAM (5% larger, $>1.5$), the axial position is located at ~52°S (Figure 11d). Larger changes in the local wind stress during extreme SAM events are experienced at the northern and southern lobes of the westerlies, at 35°S–45°S and 50°S–60°S, respectively (Figure 11e). For example, the wind stress residuals between 35°S and 45°S (50°S–60°S) have a correlation of −0.43 (0.45) with the SAM index at time scales longer than one year, which indicates that the large-scale

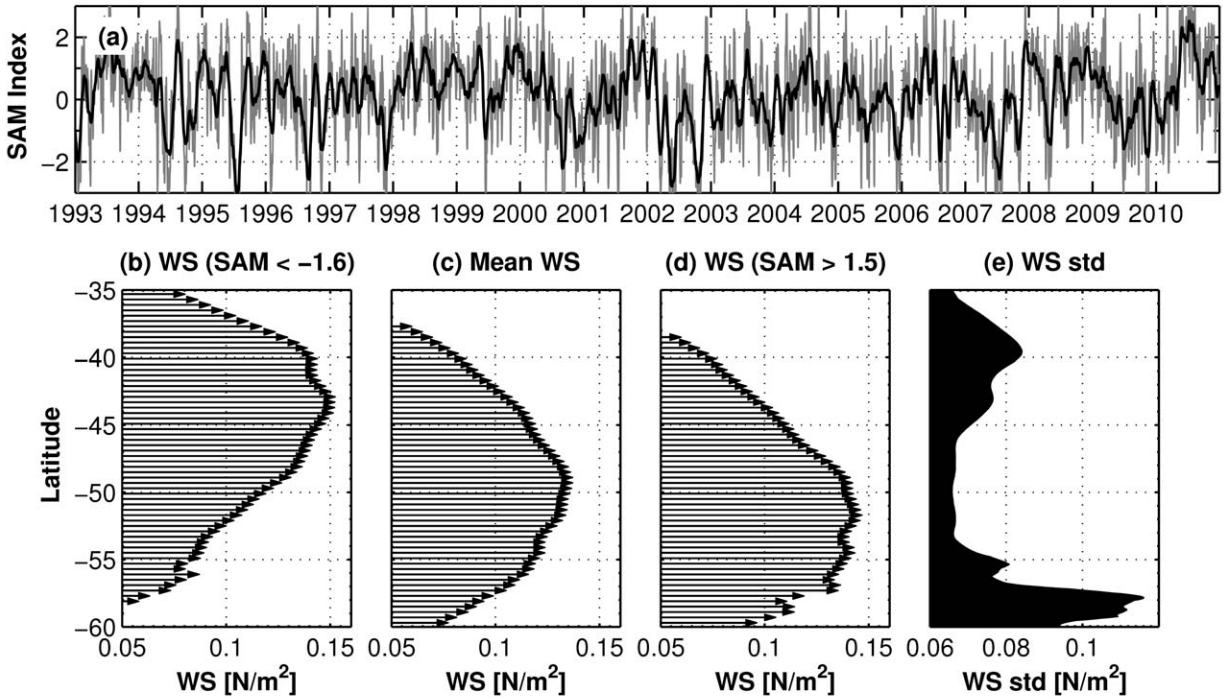


**Figure 11.** (a) SAM daily (gray line) and monthly low-passed (black line) index. Average wind stress structure (b) during periods of extreme negative SAM ($<-1.6$), (c) during 1993–2010, and (d) during periods of extreme positive SAM ($>1.5$). SAM-related wind stress standard deviation.

SAM drive interannual changes in the structure of local wind stress south of Africa. This is further supported by the wavelet transform of these time series. Long period variability is observed for the SAM index (Figure 3f), for the wind stress between 35°S and 45°S (Figure 3g), and between 50°S and 60°S (Figure 3h), indicating that periods longer than annual are a significant component of the atmospheric variability. As the dominant mode of atmospheric variability in the southern ocean, the SAM accounts for ~20% of the zonal wind stress variance south of Africa. Other mechanisms such as (i) atmospheric waves [*Hartmann and Lo*, 1998], (ii) the El Nino Southern Oscillation [*Garreaud and Battisti*, 1999], and (iii) local effects, may also contribute to the zonal wind stress variability in the region.

Observations indicate that the SAM-related changes in the wind stress are first observed between 35°S and 45°S (not shown here). The variability of the wind stress residuals between 35°S and 45°S, of the SST residuals between 45°S and 55°S, and of the SAF and APF frontal transports sometimes exhibits periods longer than annual (Figure 3). Results indicate that the meridionally averaged wind stress residuals between 35°S and 45°S have significant negative correlations with the averaged SST residuals between 45°S and 55°S (Figure 12a). These significant correlation coefficients are obtained for lags of 0–25 weeks, indicating that changes in the wind stress precede or coincide with changes in the upper-layer temperature between, at all frequencies analyzed in this work. Significant negative correlations between these two time series are also obtained for lags of ~2 years, which is consistent with a delayed response due to the eddy field as suggested by previous studies [*Meredith and Hogg*, 2006]. The negative correlations indicate that low values of wind stress residuals (easterlies anomalies) between 35°S and 45°S are linked with a warmer upper-layer between 45°S and 55°S. The wind stress residuals also have significant positive (negative) correlations with the SAF (APF) transport (Figures 12b and 12c), indicating that a lower wind stress residual between 35°S and 45°S is linked with a lower (higher) SAF (APF) transport. The highest correlation coefficients between the wind stress residuals and the frontal transports are obtained for a positive lag centered at ~10–20 weeks, which shows that the changes in the wind stress precede the changes in the SAF and APF transports. The correlation coefficients between the wind stress and the oceanic parameters analyzed here increase with increasing low-pass filter width (Figure 12). The forcing mechanism linking these parameters will be discussed in the next section.

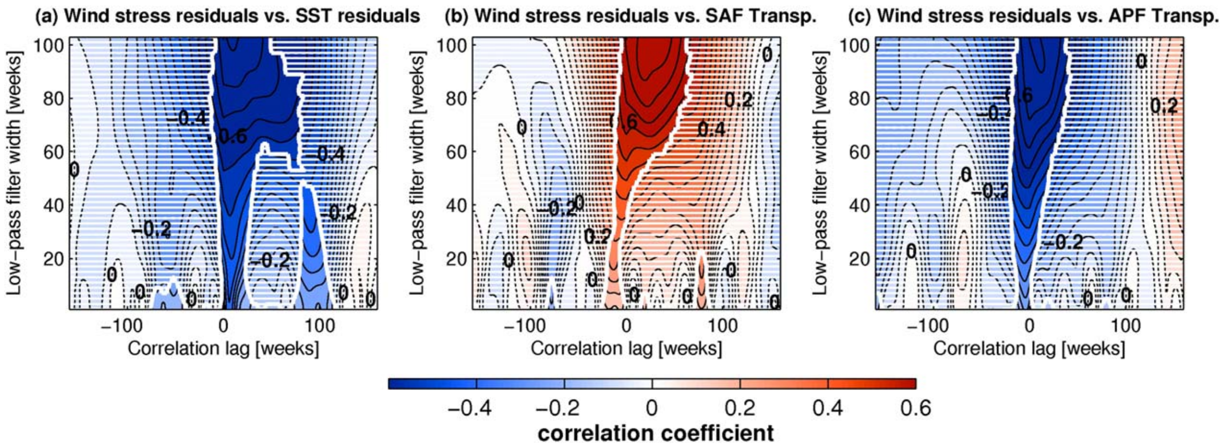


**Figure 12.** Correlation coefficients between: (a) the averaged wind stress between 35°S and 45°S, and the averaged SST between 45°S and 55°S; (b) the averaged wind stress between 35°S and 45°S, and the SAF transport; and (c) the averaged wind stress between 35°S and 45°S, and the APF transport. Each diagram is as described in Figure 10.

## 5. Discussion

In this section, the links observed between the variability in the upper-ocean thermal structure, the frontal transports of the SAF and APF, and the wind stress variability in the region between South Africa and Antarctica, are discussed. The goal here is to investigate a consistent mechanism connecting the upper-ocean dynamics to the atmospheric variability in this region. Previous studies demonstrated that changes in the structure and intensity of the westerlies may cause an immediate and/or a delayed response of the ACC. The immediate response of the ACC to the changes in the overlying wind stress occurs through Ekman dynamics. For example, the southward displacement of the westerlies causes adjustments in the Ekman layer that result in horizontal advection and vertical subduction [*Gupta and England*, 2006; *Downes et al*., 2011]. Even though the observed easterly anomalies between 35°S and 45°S are usually not linked with a change in the direction of the wind, changes in the Ekman balance are still expected. This mechanism drives meridional excursions of the ACC fronts in places of relatively flat bottom topography [*Sallee et al*., 2008]. The delayed response of the ACC occurs as follows [*Meredith and Hogg*, 2006]: the excess of wind energy is slowly transferred from the upper-layer to the lower-layers through an eddy regime, and these changes in the eddy field increase the poleward heat flux [*Hogg et al*., 2008]. The results presented here also show evidence of a delayed ocean response to changes in the westerlies (section 4.1). However, the signal related to an immediate response in the ACC (0–25 weeks) is much stronger. In addition, since this study is focused on the regional variability, remote sources of variability are not presented here. Therefore, the analysis developed here focuses on the local mechanism driving the immediate ACC response to the changes in the overlying wind stress.

The correlations presented in section 4.6 indicate that the variability of the upper-ocean temperature and the SAF and APF frontal transports may be linked to the wind stress at time scales longer than annual, suggesting a dynamic and integrated response of the ocean to the changes in the forcing. It is worth noting here that, even though the correlations indicate relatively short response times (0–25 weeks), the time scales of the processes involved are longer than annual. The SST (section 4.1) has a year-to-year variability in the ACC region between 45°S and 55°S that is consistent with the variability of the local wind stress. The negative correlation between these SST residuals and the local wind stress residuals between 35°S and 45°S indicates that a weakening in the zonal wind is linked to a warmer SST in the ACC. The weakening of the zonal wind stress between 35°S and 45°S during positive SAM is linked with the southward displacement of the westerlies, causing the development of poleward Ekman transport anomalies. These poleward anomalies represent a weakening of the actual Ekman transport to the north due to the prevailing direction of the westerlies, and cause the advection of warmer waters to the south, which is in agreement with the observed warm SST residuals between 45°S and 55°S during 1994–1996, 2001–2002, 2006, 2008, and 2009–2010 (Figures 13a and 13b). In addition, the observed subsurface temperature (Figures 4d and 5, section 4.2) has shown that the vertical extent of these warm anomalies in the ACC were confined to the upper 100

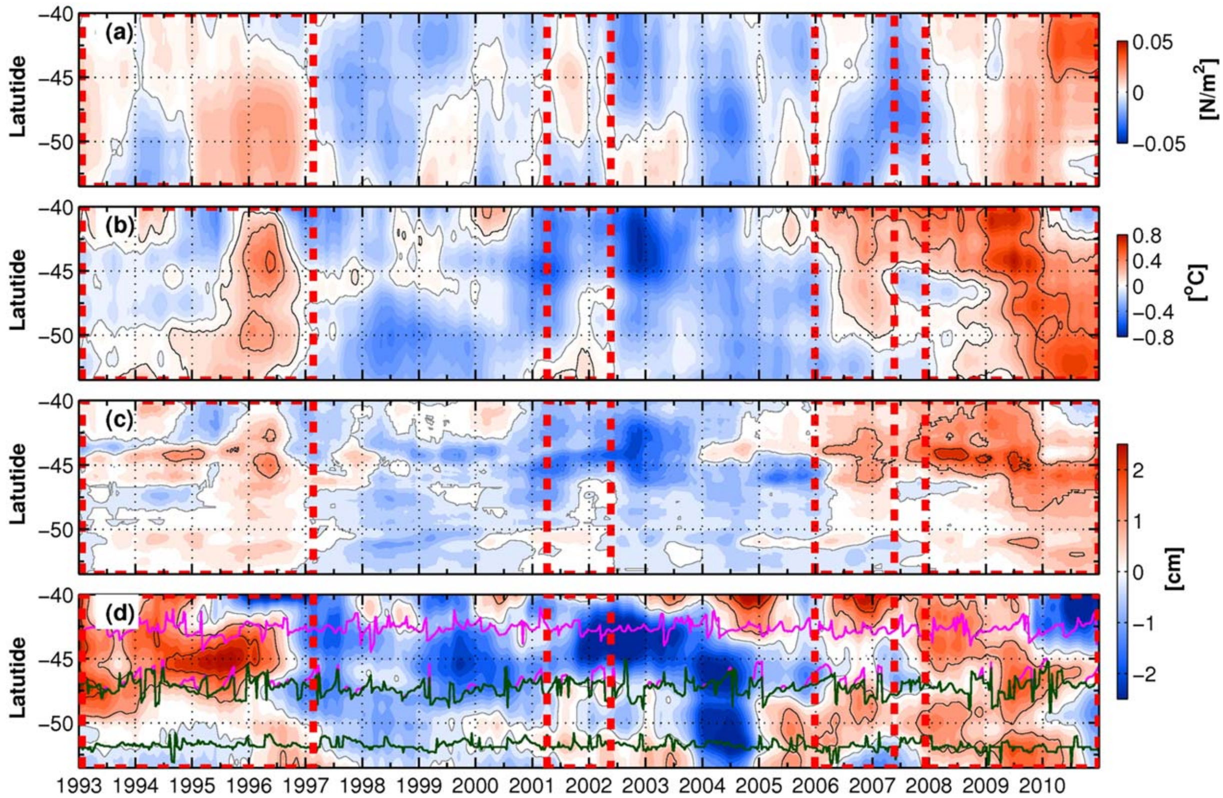


**Figure 13.** One year low-passed residuals (seasonal cycle removed) time series along AX25 for the: (a) wind stress multiplied by −1 (for visual purposes), (b) SST, (c) $\eta_{ek+sst}$, and (d) altimetry-derived SHA. The thick red dashed line highlights the periods of the warm SST residuals. Black contours in Figure 13b every 0.2°C highlight positive SST residuals, and in Figures 13b and 13c every 1 cm highlight positive SHA residuals. The magenta and green lines in Figure 13c delimit the SAF and APF frontal domains, respectively.

m, which is the average mixed layer depth in the region [*Boyer et al*., 2004; *Sallée et al*., 2010] and also coincides with estimates of the Ekman layer depth in other regions of the Southern Ocean [*Lenn and Chereskin*, 2009]. The subsurface warming confined to the upper-layer is illustrated here by the February 2010 XBT realization (Figures 4c and 4d). Evidence of Ekman drift-derived salinity anomalies along AX25 has also been presented for the southern half of the SAF domain by a previous study [*Gladyshev et al*., 2008]. Therefore, these results show that adjustments in prevailing winds at the region cause thermodynamic changes in the mixed layer, confirming the strong SST signature due to SAM observed by a previous study [*Gupta and England*, 2006]. The positive correlation between the SAM index and the APF heat content, described in a previous study [*Swart and Speich*, 2010] for the same region, is likely caused by the mechanism described here.

While the warm SST events illustrate the thermodynamic response of the ACC to wind forcing through southward advection of warm waters by anomalous Ekman transports, the correlations between the frontal transports and the wind stress suggest that these changes may also influence the ACC dynamics. Around the Antarctic continent, the integrated ACC transport adjusts to changes in the zonal wind stress within a couple of days through fast propagating barotropic waves [*Hughes et al*., 1999; *Gille* et al., 2001; *Webb and De Cuevas*, 2007]. However, the results evaluated here suggest that the local atmospheric forcing component is of relevance for the transport structure, driving the SAF and APF transport to respond differently. The observed opposite response of the SAF and APF transports is due to the specific latitudinal ranges of these fronts, which expose them to distinct dynamical regimes [*Sallee et al*., 2008]. Therefore, it is suggested here that the meridional changes in the wind stress are linked to changes in the dynamic height distribution along AX25, driving a specific frontal transport response through geostrophy.

The variability in the dynamic height can be caused by several factors, including changes in the water density, and by the wind forcing [*Vivier et al*., 1999]. Two potential mechanisms are

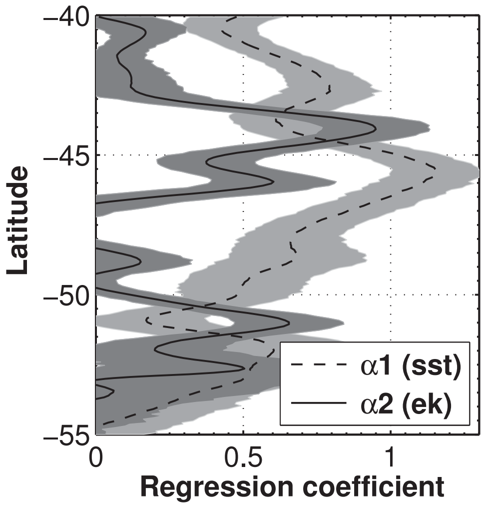


**Figure 14.** Regression coefficients for the multivariate linear regression model: SSHA = $\alpha_1\eta_{sst} + \alpha_2\eta_{ek}$, where $\eta_{sst}$ is thermosteric component, and $\eta_{ek}$ is the Ekman pumping component. The 95% confidence levels (shaded areas) are estimated using a bootstrap approach [*Johnson*, 2001].

investigated here for time scales longer than annual. The first mechanism is through the development of Ekman pumping anomalies due to meridional changes in the structure of the wind, which can cause the development of convergence (divergence) in the Ekman layer [*Hall and Visbeck*, 2002; *Gupta and England*, 2006]. The negative (positive) Ekman pumping anomalies cause an increase (decrease) in the sea level. The contribution of the local Ekman pumping to the SSHA signal ($\eta_{ek}$) is estimated using a previously reported method [*Cabanes et al.*, 2006]:

$$\frac{\partial \eta_{ek}}{\partial t} = -A\nabla\times\left(\frac{\tau}{\rho_o f}\right),\ A=\frac{1}{g}\int_{-H}^{0} N^2\left(1+\frac{z}{H}\right)\partial z. \tag{1}$$

Here, $\rho_o$ is the reference seawater density, f is the Coriolis parameter, N is the Brunt–Väisälä frequency, and H is the reference level, which is set to 100 m. The second mechanism evaluated here is the development of thermosteric-induced sea level changes, where the southward advected temperature residuals in the Ekman layer may cause the thermal expansion of the water, corresponding to an indirect response of the sea level to the wind forcing. The thermosteric changes to the sea level are estimated here using:

$$\eta_{sst} = \int_{-z}^{0} \delta(S_o, T, z)\partial z - \int_{-z}^{0} \delta(S_o, T_o, z)\partial z \tag{2}$$

where Z is set to 100 m, and $S_o$ and $T_o$ are the mean salinity and temperature structure along AX25, respectively. It should be noted here that $\eta_{ek}$ and $\eta_{sst}$ are computed based on residual variables, making them anomalous quantities with respect to the seasonal cycle. The relative effect of $\eta_{ek}$ and of $\eta_{sst}$ on the dynamic height is quantified here using a latitude dependent multivariate linear regression method to determine the slope coefficients ($\alpha_1$ and $\alpha_2$) of the equation: $SSHAr=\alpha_1\eta_{sst}+\alpha_2\eta_{ek}$, where SSHAr stands for the SSHA residuals. Values for $\alpha_1$ and $\alpha_2$ are determined as a function of the latitude (Figure 14). In general, the slope coefficient $\alpha_1$ is larger than $\alpha_2$, indicating the dominant contribution of the thermosteric component to the SSHA variability. Previous studies using in situ observations demonstrated that the SSHA is well correlated with the steric height [*Guinehut et al.*, 2006] and with the heat content [*Willis et al.*, 2004] in this region of the Southern Ocean, which indicates that the subsurface density and thermal structure is intimately linked with the SSHA variability. In fact, a previous analysis in the Pacific sector of the ACC has shown that usually the Ekman pumping has a secondary effect on the SSHA variability [*Vivier et al.*, 1999]. However, values for $\alpha_2$ indicate that the Ekman pumping is also of relevance in some latitude bands, specially centered at 44°S and 51°S, where values of $\alpha_2$ are larger than $\alpha_1$. These latitude bands are off the mean axial position of the westerlies (~49°S), where larger values for the wind stress curl are usually observed. Therefore, this result is consistent with the dynamics of the region, emphasizing the direct sea level response to the changes in the overlying wind stress.

The total residual sea level signal formed by the Ekman pumping and the thermosteric components ($\eta_{ek+sst}=\alpha_1\eta_{sst}+\alpha_2\eta_{ek}$) ranges between −2 and 2 cm (Figure 13c). The pattern exhibited by $\eta_{(ek+sst)}$ is in good agreement (r = 0.6) with the observed SSHA residuals (Figure 13d), and also shows similar positive

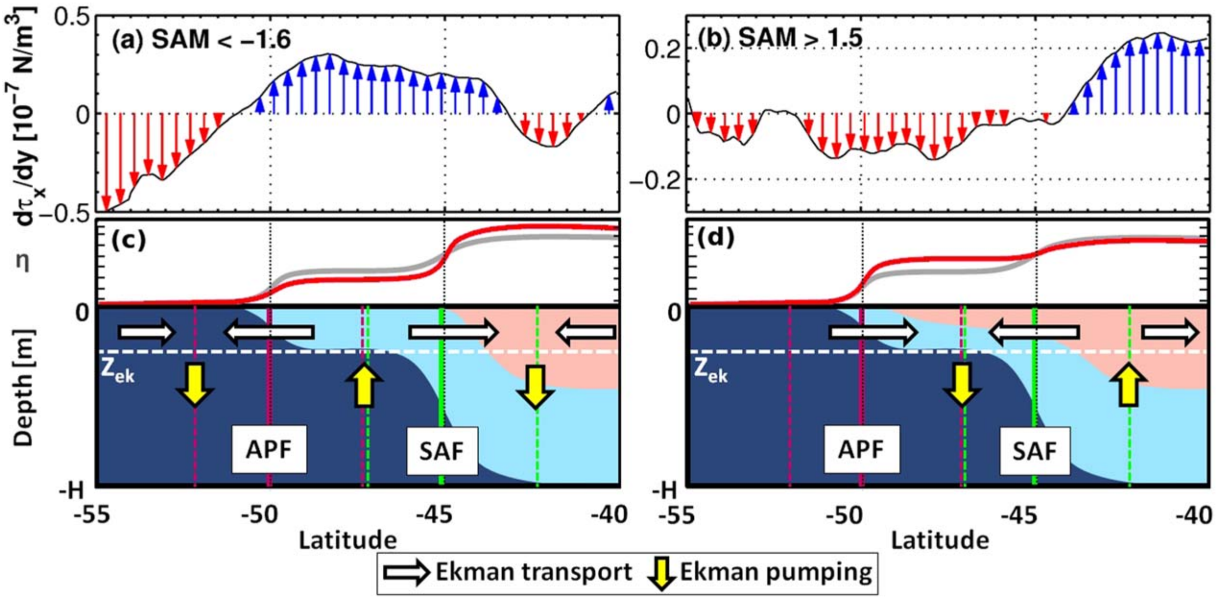


**Figure 15.** Ekman pumping anomalies during periods of (a) extreme negative and of (b) extreme positive SAM. Schematic representation of the SAF and APF dynamical response to local changes in the wind stress during periods of Figure 15c extreme negative and of Figure 15d extreme positive SAM. $Z_{ek}$ and $\eta$ represent the symbolic depth of the Ekman layer and the dynamic height, respectively. In Figures 15c and 15d, the solid gray (red) line represents the climatological dynamic height (adjusted dynamic height during periods of extreme SAM), the solid magenta (green) line represents the location of the APF (SAF), and the dashed magenta (green) lines represent the boundaries of the APF (SAF) frontal region. Note that the location of the APF and SAF (maximum dynamic height gradient) is insensitive to the SAM.

values during the periods of the warm events (1994–1996, 2001–2002, 2006, 2008, and 2009–2010), indicating that the low-frequency SSHA variability is largely due to a combination of the Ekman pumping with thermosteric anomalies. Other components, such as local density variations due to salinity, and horizontal advection, may account for the unexplained SSHA variability.

Even though thermosteric changes have an important role on the SSHA variability, this component (as computed here), is only linked to changes in the pressure gradient on the upper 100 m, which has an insignificant contribution to the SAF and APF frontal transports. The Ekman pumping component, on the other hand, is linked to changes in the pressure gradient in the entire water column, which is relevant to the frontal transports. The larger contribution of the Ekman pumping to the zonal transports has been acknowledged by a previous study [*Gupta and England*, 2006]. The Ekman pumping component drives SSHA variability in latitude bands that coincide with the SAF and APF frontal boundaries, suggesting that the Ekman pumping may provide the link between the wind stress and the frontal transports. To verify this, Ekman pumping anomalies during periods of extreme SAM ($<-1.6$ or $>1.5$) are evaluated (Figure 15). During periods of extreme positive SAM ($>1.5$), positive Ekman pumping anomalies are observed on the SAF northern boundary, while negative Ekman pumping anomalies are observed on the SAF-APF boundary, which is consistent with the generation of a dynamic height gradient linked with lower (higher) SAF (APF) transport. During periods of extreme negative SAM ($<-1.6$), the observed Ekman pumping anomalies are also consistent with a higher (lower) SAF (APF) transport. Therefore, these results indicate that Ekman pumping anomalies account for the generation of the dynamic height gradient driving low frequency variability of the SAF and APF transport. At higher frequencies, smaller correlation coefficients between the wind stress and the frontal transports (Figure 12) imply that other processes (e.g., mesoscale activity) dominate.

Previous studies have emphasized the role of ocean eddies for maintaining a stable ACC transport under increased westerlies conditions [*Hallberg and Gnanadesikan*, 2006; *Hogg et al.*, 2008; *Screen et al.*, 2009]. Results shown here indicate that SAM-related changes in the local structure of the westerlies may also have a small impact upon the net ACC transport because of the opposite responses of the SAF and APF transports. As presented above, the relationship between the SAF and APF transport has a slope of $-0.8$, which indicates that an increase in the APF transport coincides with a decrease in the SAF transport. This response is observed, for example, during the 2002 warm event, when the SAF transport was reduced by ~7 Sv, while the APF transport was increased by ~6 Sv. Therefore, even though the integrated wind stress around

Antarctica sets up the mean ACC transport [*Webb and De Cuevas*, 2007], results analyzed here show that the local wind stress can modulate its meridional structure.

While specific long-term consequences of the local mechanism reported here are unclear, these thermodynamic changes in the ACC may be linked with other processes of global relevance. For instance, the SAM-related wind-driven warming of the ACC Ekman/mixed layer observed here is potentially linked with the development of positive heat content anomalies in the region [*Swart and Speich*, 2010]. Given the significant positive trend in the SAM index during past decades [*Marshall*, 2003], the mechanism described here may have provided one source for the observed ACC warming during this period [*Gille*, 2002, 2008]. The ACC warming has a wide range of implications for the global climate and ecosystems. In addition to the warming of this current, the Ekman pumping anomalies described here are known to drive changes in the subduction rate of water masses in the Southern Ocean. According to a previous study [*Gupta and England*, 2006], the Ekman divergence-convergence-divergence pattern linked with positive SAM generates anomalous vertical motion that extends to depths exceeding 4000 m, enhancing the Deacon cell and shifting its center southward. Changes in the Deacon cell potentially affect the intermediate water ventilation and the Meridional Overturning Circulation. Finally, the changes in the frontal transports observed here may also be linked with changes in the Atlantic-Indian exchanges of heat and mass, because different fronts are associated with different water masses [*Downes et al*., 2011]. Further studies may yield additional insightful information.

In contrast with the frontal transports, the SAF and APF locations (sections 4.4 and 4.5, respectively) exhibit no significant correlations with the wind stress and with the SAM index, which is consistent with previous observations in the region [*Sallee et al*., 2008; *Billany et al*., 2010]. The absence of significant correlations between the frontal locations and the atmospheric variability indicates that processes other than winds are important for driving the meridional displacements (meandering) of the SAF and APF in this region. Previous studies demonstrated that the location of the ACC fronts is only controlled by the atmospheric forcing in the absence of topographic features [*Sallee et al*., 2008], which is not the case south of Africa. Both the APF and SAF cross the Mid-Ocean Ridge upstream of AX25 (Figure 1), which may cause the generation of baroclinic instabilities through alterations in the mean flow forced by the topography [*Thompson and Richards*, 2011, *Swart and Speich*, 2010]. The generation of baroclinic instabilities may potentially explain the observed SAF and APF meandering between 6°W and 6°E, even though the APF is likely to be partially steered by the topography. Therefore, the SAF and APF frontal motions in this region are likely controlled by the topography through the generation of baroclinic instabilities, which have been shown to drive significant high-frequency changes in the heat content of the region [*Swart and Speich*, 2010]. Further studies are still needed to clarify the full extent and stability of this mechanism.

## 6. Conclusions

Using hydrographic and satellite observations, a new mechanism is reported, by which the local atmospheric variability forces a dynamic response of the ocean in the ACC region. This mechanism has been determined through the analysis of different components of the oceanic variability in the region between South Africa and Antarctica. In this region, the meridional changes in the westerlies are dominated by the SAM. The negative (positive) correlation between the SAM and the wind stress between 35°S and 45°S (50°S–60°S) is indicative of the southward displacement of the westerlies during positive SAM phases. These changes in the wind stress are shown to play an important role for the local oceanic variability, as the observations suggest that the ocean responds almost immediately through Ekman dynamics.

The main finding of this work is that in the study region, even though other factors (e.g., topography) control the ACC frontal motions, the wind field drives temperature anomalies in the Ekman layer and frontal transport variability through Ekman dynamics. Positive temperature residuals were observed in the upper $\sim$100 m and were detected during 1994–1996, 2001–2002, 2006, 2008, and 2009–2010 in the ACC region. These warm temperature residuals are linked to positive SAM-related changes in the westerlies and are caused by anomalous poleward Ekman transport. Significant negative correlations between the SST residuals in the ACC region and the averaged wind stress at 35°S–45°S emphasize this link.

In addition, the variability of the wind stress is significantly correlated with the APF and SAF transports, suggesting a dynamical response of the ACC to local changes in the westerlies at time scales longer than annual. The observed changes in the frontal transports are caused by dynamic height adjustments. Results showed that, even though the thermosteric component also plays an important role in the SSHA variability of the region, Ekman pumping anomalies near the SAF and APF boundaries causes the development of SSHA anomalies that are ultimately linked with changes in the geostrophic transport of these fronts. These changes in the structure of the westerlies drive an opposite response on the SAF and APF, because their specific latitude range exposes them to different Ekman pumping anomalies. For example, the Ekman divergence-convergence-divergence pattern during positive SAM is linked with less (more) intense SAF (APF) transport. The opposite response from the SAF and APF transports to local changes in the westerlies indicates that such changes in the wind forcing may have a small impact in the net ACC transport. At higher frequencies, other components (e.g., mesoscale variability) of the dynamics seem to play a more important role.

This study analyzed hydrographic and satellite observations to report a potential mechanism by which the local atmospheric forcing drives changes in the ACC structure through an integrated response in the upper-layer. It is highlighted here the importance of each component of the global observing system. While the repeat XBT transects provide eddy-permitting temperature sections during the summer months, T-S profiles from Argo floats are available year round to fill the seasonal temporal gaps not sampled by XBTs and to provide water density observations needed for dynamic height computations. In addition, satellite altimetry, winds, and SST are continuously available with high-resolution data that can be combined with the hydrographic observations to extend the analysis back to the beginning of the altimetry period. The results of this study emphasize the value of sustained XBT observations along the AX25 repeat hydrographic transect, and of the other components of the observing system in this region.

**Acknowledgments**
Argo and CTD profiles were obtained from the Global Temperature-Salinity Profile Programme (http://www.nodc.noaa.gov/GTSPP). The altimetry products were produced by Ssalto/Duacs, distributed by AVISO, and supported by the CNES. NOAA High Resolution SST data were provided by the NOAA/OAR/ESRL PSD, Boulder, Colorado, USA (http://www.esrl.noaa.gov/psd/). The XBT data are made freely available by the Atlantic Oceanographic and Meteorological Laboratory (http://www.aoml.noaa.gov/phod). The authors would like to thank Silvia Garzoli, Qi Yao, Claudia Schmid, Marlos Goes, and Francis Bringas for the discussions on the data analysis, and Molly Baringer, Elizabeth Johns, and Gregory Foltz for helpful suggestions on the manuscript. The South African National Antarctic Programme (SANAP) and the University of Cape Town are also acknowledged for their continued support in undertaking the research voyages along the AX25/GoodHope transect. The authors would also like to thank the three anonymous reviewers for the insightful comments and suggestions. This research was carried out under the auspices of the Cooperative Institute for Marine and Atmospheric Studies (CIMAS), a joint institute of the University of Miami and the National Oceanic and Atmospheric Administration (NOAA), Cooperative Agreement NA17RJ1226. This work was funded by the NOAA Climate Program Office and by the NOAA Atlantic Oceanographic and Meteorological Laboratory.

## References


Alory, G., S. Wijffels, and G. Meyers (2007), Observed temperature trends in the Indian Ocean over 1960–1999 and associated mechanisms, *Geophys. Res. Lett.*, *34*, L02606, doi:10.1029/2006GL028044.

Ansorge, I., S. Speich, J. Lutjeharms, G. Goni, C. Rautenbach, P. Froneman, M. Rouault, and S. Garzoli (2005), Monitoring the oceanic flow between Africa and Antarctica: Report of the first GoodHope cruise, *S. Afr. J. Sci.*, *101*(1 & 2), 29–35.

Atlas, R., R. Hoffman, J. Ardizzone, S. Leidner, J. Jusem, D. Smith, and D. Gombos (2011), A cross-calibrated, multiplatform ocean surface wind velocity product for meteorological and oceanographic applications, *Bull. Am. Meteorol. Soc.*, *92*, 157–174.

Baringer, M., and S. Garzoli (2007), Meridional heat transport determined with expendable bathythermographs–part I: Error estimates from model and hydrographic data, *Deep Sea Res., Part I*, *54*(8), 1390–1401.

Bailey, R., A. Gronel, H. Phillips, G. Meyers, and E. Tanner (1994), CSIRO Cookbook for quality control of expendable bathythermograph (XBT) data, *Rep. 220*, 75 pp., CSIRO Mar. Lab., Hobart, Australia.

Belkin, I., and A. Gordon (1996), Southern ocean fronts from the Greenwich Meridian to Tasmania, *J. Geophys. Res.*, *101*(C2), 3675–3696.

Bi, D., W. Budd, A. Hirst, and X. Wu (2002), Response of the Antarctic Circumpolar Current transport to global warming in a coupled model, *Geophys. Res. Lett.*, *29*(24), 2173, doi:10.1029/2002GL015919.

Billany, W., S. Swart, J. Hermes, and C. Reason (2010), Variability of the southern ocean fronts at the Greenwich Meridian, *J. Mar. Syst.*, *82*(4), 304–310.

Boebel, O., J. R. E. Lutjeharms, C. Schmid, W. Zenk, T. Rossby, and C. Barron (2003), The Cape Cauldron: A regime of turbulent inter-ocean exchange, *Deep Sea Res., Part II*, *50*, 57–86.

Boning, C. W., A. Dispert, M. Visbeck, S. Rintoul, and F. Schwarzkopf (2008), The response of the Antarctic Circumpolar Current to recent climate change, *Nat. Geosci.*, *1*(12), 864–869.

Boyer, C., G. Madec, A. S. Fischer, A. Lazar, and D. Iudicone (2004), Mixed layer depth over the global ocean: An examination of profile data and a profile-based climatology, *J. Geophys. Res.*, *109*, C12003, doi:10.1029/2004JC002378.

Cabanes, C., T. Huck, and C. de Verdière (2006), Contributions of wind forcing and surface heating to interannual sea level variations in the Atlantic Ocean, *J. Phys. Oceanogr.*, *36*(9), 1739–1750.

Daneshzadeh, Y.-H. C., J. F. Festa, and S. M. Minton (1994), Procedures used at NOAA-AOML to quality control real time XBT data collected in the Atlantic Ocean, *NOAA Tech. Memo, ERL AOML-78*, 44 pp., NOAA Atl. Oceanogr. and Meteorol. Lab, Miami, Fla.

Dencausse, G., M. Arhan, and S. Speich (2011), Is there a continuous subtropical front south of Africa?, *J. Geophys. Res.*, *116*, C02027, doi:10.1029/2010JC006587.

Dong, S., J. Sprintall, and S. Gille (2006), Location of the Antarctic polar front from AMSRE satellite sea surface temperature measurements, *J. Phys. Oceanogr.*, *36*(11), 2075–2089.

Downes, S., A. Budnick, J. Sarmiento, and R. Farneti (2011), Impacts of wind stress on the Antarctic Circumpolar Current fronts and associated subduction, *Geophys. Res. Lett.*, *38*, L11605, doi:10.1029/2011GL047668.

Foufoula-Georgiou, E., and P. Kumar (1994), *Wavelets in geophysics*, vol. *4*, 373 pp., Academic, San Diego, Calif.

Fyfe, J., and O. Saenko (2006), Simulated changes in the extratropical Southern Hemisphere winds and currents, *Geophys. Res. Lett.*, *33*, L06701, doi:10.1029/2005GL025332.

Fyfe, J. C., O. Saenko, K. Zickfeld, M. Eby, and A. Weaver (2007), The role of poleward-intensifying winds on Southern Ocean warming, *J. Clim.*, *20*(21), 5391–5400.

Garreaud, R., and D. S. Battisti (1999), Interannual (ENSO) and interdecadal (ENSO-like) variability in the Southern Hemisphere tropospheric circulation, *J. Clim.*, *12*(7), 2113–2123.

Gille, S. (2002), Warming of the Southern Ocean since the 1950s, *Science*, *295*(5558), 1275–1277.

Gille, S. (2008), Decadal-scale temperature trends in the Southern Hemisphere ocean, *J. Clim.*, *21*(18), 4749–4765.
Gille, S., D. Stevens, R. Tokmakian, and K. Heywood (2001), Antarctic circumpolar current response to zonally averaged winds, *J. Geophys. Res*, *106*(C2), 2743–2759.
Gladyshev, S., M. Arhan, A. Sokov, and S. Speich, S. (2008), A hydrographic section from South Africa to the southern limit of the Antarctic Circumpolar Current at the Greenwich Meridian, *Deep Sea Res., Part I*, *55*(10), 1284–1303.
Goni, G. J., F. Bringas, and P. N. DiNezio (2011), Observed low frequency variability of the Brazil Current front, *J. Geophys. Res.*, *116*, C10037, doi:10.1029/2011JC007198.
Grinsted, A., J. Moore, and S. Jevrejeva (2004), Nonlinear processes in geophysics application of the cross wavelet transform and wavelet coherence to geophysical time series, *Nonlinear Process. Geophys.*, *11*, 561–566.
Guinehut, S., P. Y. Le Traon, and Larnicol, G. (2006). What can we learn from global altimetry/hydrography comparisons?, *Geophys. Res. Lett.*, *33*, L10604, doi:10.1029/2005GL025551.
Gupta, A., and M. England (2006), Coupled ocean–atmosphere–ice response to variations in the southern annular mode, *J. Clim.*, *19*, 4457–4486.
Hall, A., and M. Visbeck (2002), Synchronous variability in the southern hemisphere atmosphere, sea ice, and ocean resulting from the annular mode, *J. Clim.*, *15*(21), 3043–3057.
Hallberg, R., and A. Gnanadesikan (2006), The role of eddies in determining the structure and response of the wind-driven Southern Hemisphere overturning: Results from the modeling eddies in the Southern Ocean (MESO) project, *J. Phys. Oceanogr.*, *36*(12), 2232–2252.
Hartmann, D. L., and F. Lo (1998), Wave-driven zonal flow vacillation in the Southern Hemisphere. *J. Atmos. Sci.*, *55*(8), 1303–1315.
Hogg, A., M. Meredith, J. Blundell, and C. Wilson (2008), Eddy heat flux in the Southern Ocean: Response to variable wind forcing, *J. Clim.*, *21*(4), 608–620.
Hughes, C. W., M. P. Meredith, and K. J. Heywood (1999), Wind-driven transport fluctuations through Drake Passage: A southern mode, *J. Phys. Oceanogr.*, *29*(8), 1971–1992.
Johnson, R. W. (2001), An introduction to Bootstrap, *Teaching Stat.*, *23*(2), 49–54.
Le Traon, P., and G. Dibarboure (1999), Mesoscale mapping capabilities of multiple-satellite altimeter missions, *J. Atmos. Oceanic. Technol.*, *16*(9), 1208–1223.
Le Traon, P., F. Nadal, and N. Ducet (1998), An improved mapping method of multisatellite altimeter data, *J. Atmos. Oceanic. Technol.*, *15*(2), 522–534.
Legeais, J., S. Speich, M. Arhan, I. Ansorge, E. Fahrbach, S. Garzoli, and A. Klepikov (2005), The baroclinic transport of the Antarctic Circumpolar Current south of Africa, *Geophys. Res. Lett.*, *32*(24), doi:10.1029/2005GL023271.
Lenn, Y., and T. Chereskin (2009), Observations of Ekman currents in the Southern Ocean, *J. Phys. Oceanogr.*, *39*(3), 768–779.
Lutjeharms, J. R. E. (1985), Location of frontal systems between Africa and Antarctica: Some preliminary results, *Deep Sea Res., Part A*, *32*, 1499–1509.
Lutjeharms, J. R. E. (1988), Meridional heat transport across the sub-tropical convergence by a warm eddy, *Nature*, *331*, 251–253.
Lutjeharms, J. R. E., and H. R. Valentine (1984), Southern Ocean thermal fronts south of Africa, *Deep Sea Res., Part A*, *31*, 1461 – 1475.
Marshall, G. (2003), Trends in the southern annular mode from observations and reanalyses, *J. Clim.*, *16*(24), 4134–4143.
Meredith, M. P., and A. M. Hogg (2006), Circumpolar response of Southern Ocean eddy activity to a change in the Southern Annular Mode, *Geophys. Res. Lett.*, *33*, L16608, doi:10.1029/2006GL026499.
Orsi, A. H., T. Whitworth, and W. D. Nowlin (1995), On the meridional extent and fronts of the Antarctic Circumpolar Current, *Deep Sea Res., Part I*, *42*(5), 641–673.
Reynolds, R., T. Smith, C. Liu, D. Chelton, K. Casey, and M. Schlax (2007), Daily high-resolution-blended analyses for sea surface temperature, *J. Clim.*, *20*, 5473–5496.
Rintoul, S., and S. Sokolov (2001), Baroclinic transport variability of the Antarctic Circumpolar Current south of Australia (WOCE repeat section SR3), *J. Geophys. Res.*, *106*(C2), 2815–2832.
Rio, M., S. Guinehut, and G. Larnicol (2011), New CNES-CLS09 global mean dynamic topography computed from the combination of grace data, altimetry, and in situ measurements, *J. Geophys. Res*, *116*, C07018, doi:10.1029/2010JC006505.
Saenko, O., J. Fyfe, and M. England (2005), On the response of the oceanic wind-driven circulation to atmospheric $CO_2$ increase, *Clim. Dyn.*, *25*(4), 415–426.
Sallee, J., K. Speer, and R. Morrow (2008), Response of the Antarctic Circumpolar Current to atmospheric variability, *J. Clim.*, *21*(12), 3020–3039.
Sallée, J. B., K. G. Speer, and S. R. Rintoul (2010), Zonally asymmetric response of the Southern Ocean mixed-layer depth to the southern annular mode, *Nat. Geosci.*, *3*(4), 273–279.
Schmid, C. (2005), Impact of combining temperature profiles from different instruments on an analysis of mixed layer properties, *J. Atmos. Oceanic. Technol.*, *22*(10), 1571–1587.
Screen, J., N. Gillett, D. Stevens, G. Marshall, and H. Roscoe (2009), The role of eddies in the southern ocean temperature response to the southern annular mode, *J. Clim.*, *22*(3), 806–818.
Smith, W., and D. Sandwell (1997), Global sea floor topography from satellite altimetry and ship depth soundings, *Science*, *277*(5334), 1956–1962.
Sokolov, S. and S. Rintoul (2007), Multiple jets of the Antarctic Circumpolar Current south of Australia, *J. Phys. Oceanogr.*, *37*(5), 1394–1412.
Sokolov, S., and S. Rintoul (2009a), Circumpolar structure and distribution of the Antarctic Circumpolar Current fronts: 1. Mean circumpolar paths, *J. Geophys. Res.*, *114*, C11018, doi:10.1029/2008JC005108.
Sokolov, S., and S. Rintoul (2009b), Circumpolar structure and distribution of the Antarctic Circumpolar Current fronts: 2. Variability and relationship to sea surface height, *J. Geophys. Res.*, *114*, C11019 doi:10.1029/2008JC005248.
Sprintall, J. (2008), Long-term trends and interannual variability of temperature in Drake Passage, *Prog. Oceanogr.*, *77*(4), 316–330.
Stephens, C., J. Antonov, T. Boyer, M. Conkright, R. Locarnini, T. O'Brien, and H. Garcia (2002), World Ocean Atlas 2001, in *Temperatures, NOAA Atlas NESDIS 49*, vol. *1*, edited by S. Levitus, 176 pp., U.S. Gov. Print. Off., Washington, D. C.
Swart, S., and S. Speich (2010), An altimetry-based gravest empirical mode south of Africa: 2. Dynamic nature of the Antarctic Circumpolar Current fronts, *J. Geophys. Res.*, *115*, C03003, doi:10.1029/2009JC005300.
Swart, S., S. Speich, I. Ansorge, G. Goni, S. Gladyshev, and J. Lutjeharms (2008), Transport and variability of the Antarctic Circumpolar Current south of Africa, *J. Geophys. Res.*, *113*, C09014, doi:10.1029/2007JC004223.
Swart, S., S. Speich, I. Ansorge, and J. Lutjeharms (2010), An altimetry-based gravest empirical mode south of Africa: 1. Development and validation, *J. Geophys. Res.*, *115*, C03002, doi:10.1029/2009JC005299.

  

10.1002/2013JC008908

Thompson, A. F., and K. J. Richards (2011), Low frequency variability of Southern Ocean jets, *J. Geophys. Res.*, *116*, C09022, doi:10.1029/2010JC006749.

Thompson, D.W. J., and J. M. Wallace, (2000), Annular modes in the extratropical circulation. Part I: Month-to-month variability, *J. Clim.*, *13*, 1000–1016.

Thompson, D. W. J., and S. Solomon (2002), Interpretation of recent Southern Hemisphere climate change, *Science*, *296*, 895 – 899.

Vivier, F., A. Kelly, and L. Thompson (1999), Contributions of wind forcing, waves, and surface heating to sea surface height observations in the Pacific Ocean, *J. Geophys. Res.*, *104*(C9), 20,767–20,788.

Wang, Z., T. Kuhlbrodt, and M. Meredith (2011), On the response of the Antarctic Circumpolar Current transport to climate change in coupled climate models, *J. Geophys. Res.*, *116*, C08011, doi:10.1029/2010JC006757.

Wearn R., Jr., and D. Baker Jr. (1980), Bottom pressure measurements across the Antarctic Circumpolar Current and their relation to the wind, *Deep Sea Res., Part A*, *27*(11), 875–888.

Webb, D. J., and B. A. De Cuevas (2007), On the fast response of the Southern Ocean to changes in the zonal wind, *Ocean Sci.*, *3*(3), 417–427.

Weng, H., and K. Lau (1994), Wavelets, period doubling, and time-frequency localization with application to organization of convection over the tropical western Pacific, *J. Atmos. Sci.*, *51*, 2523–2541.

Whitworth, T., and W. D. Nowlin, Jr., (1987), Water masses and currents of the Southern Ocean at the Greenwich Meridian, *J. Geophys. Res.*, *92*(C6), 6462–6476.

Willis, J. K., D. Roemmich, and B. Cornuelle, B. (2004). Interannual variability in upper ocean heat content, temperature, and thermosteric expansion on global scales, *J. Geophys. Res.*, *109*, C12036, doi:10.1029/2003JC002260.

Yang, X., R. Huang, J. Wang, and D. Wang (2008), Delayed baroclinic response of the Antarctic Circumpolar Current to surface wind stress, *Sci. Chin. Ser. D: Earth Sci.*, *51*(7), 1036–1043.